UNIVERSITY OF CALIFORNIA
RIVERSIDE

An Scanning Tunneling Microscopy and Photoelectron Spectroscopy Study of Pattern Formation and Molecule Ordering under a Variety of Interactions

A Dissertation submitted in partial satisfaction
of the requirements for the degree of

Doctor of Philosophy

in

Physics

by

Yeming Zhu

December 2013

Dissertation Committee:

Professor Ludwig Bartels, Chairperson
Professor Jing Shi
Professor Ward Beyermann

The Dissertation of Yeming Zhu is approved:

Committee Chairperson

University of California, Riverside

Acknowledgments

First of all, I want to express my thanks to my advisor, Professor Ludwig Bartels. He gives me the opportunity to start my research in this wonderful group. In my more than six years graduate career in UCR, Ludwig shows me what is the surface science, how professionally to do research as a scientist, how to use the knowledge learn in physics, chemistry, electronic engineering, and machine shop to maintain, optimize the experiments, analysis the experiment results and understand, explain and predict the novel phenomena. Also, the work shows in this dissertation cannot be finished without the help from my group mates (former and current) and the co-workers from Professor Jory Yarmoffs group and Professor Jing Shis group. I am really appreciate the experiment work done by Dr. Zhihai chen, Dr. Dezheng Sun, Dr. Miaomiao Luo, KatieMarie Magnone, John Mann, Sarah. Bobek, Quan Ma, Wenhao Lu, Dr. Xiaoxiao He, and Zhiyong Wang. Also, most of the theoretical support in this dissertation is from Jonathan Wyrick, Kamelia D Cohen, Connor Holzke, Daniel Salib. As a non-native speaker, I would like to send my special thanks to my group mates Jonathan Wyrick and KatieMarie Magnone. They not only did a lot theoretical and experimental work supporting this dissertation, but also went though this tough paper which is full of grammar mistake. At the end, I want to thanks my parents, who bring me to this world and rise me up so now I can sit here to finish my Ph.D dissertation. Also, thank you my dear, Jing Xu. You are the best acquirement I get in UC Riverside.

To my parents.

My father is already sixty years old, and my mother is also fifty-five. In China, the people with similar age are already retired and have easy and relax life at home. But my presents still working hard in order to support my Ph. D life in US, and at same time dispatch the lonely life without my, or even my children as most of my school mates already have. In Chinese proverb, do not travel to distant land before the elder passing. So I appreciate my presents support, and this is the paper to demonstrate their love to me and somehow return their contribution.

ABSTRACT OF THE DISSERTATION

An Scanning Tunneling Microscopy and Photoelectron Spectroscopy Study of Pattern Formation and Molecule Ordering under a Variety of Interactions

by

Yeming Zhu

Doctor of Philosophy, Graduate Program in Physics
University of California, Riverside, December 2013
Professor Ludwig Bartels, Chairperson

Scanning tunneling microscopy (STM) is well known as a powerful instrument in surface science research. In this dissertation, STM, together with density functional theory (DFT), is used to investigate the chemical bonding properties and charge transfer of metal-organic coordination. The contribution to the coordination compounds with similar but different functional ligands having the same molecular backbones is studied. However, the STM image quality is highly related to the properties of the STM tip. How the adsorbed small molecules on the tip that lead to tip rearrangement and finally affects the STM image acquired for a long-range periodic 2-D pattern is investigated in this dissertation. Furthermore, STM is not the only instrument that can help us to understand surface science and catalysis. In this dissertation, photoelectron spectroscopies, such as XPS, PL and Raman are used to analyze the modified band gap shift of CVD grown monolayers of MoS_2, proving that low-energy argon sputtering may have significant potential for the activation, functionalization, and modification of MoS_2 layers.

Contents

List of Figures

List of Tables

Chapter 1

Introduction

It was December 2007, when I joined Professor Bartels group, as a freshman graduate student in University of California Riverside for barely three months. The first two and half years, I was working on upgrading the electronic control system for scanning tunneling microscope (STM) more like an electronic engineering student, even though I am in the department of physics & astronomy. Since full quarter of 2010, I started to work on maintaining and doing research on the Ultra-high vacuum (UHV) chamber, and a continuous flow low temperature STM following with post-doc Zhihai Chen. I had been a major contributor to two projects, and collaborated with my lab mates and the graduate students in Professor Jory Yarmoffs group and Professor Jing Shis group in three additional ones. Eight papers are published[1-8], including one first author[2].

So in this dissertation, I will go through all the works I did in the six years.

1.1 Scanning tunneling microscope

Part of this section is taken from various sources including online publications [9-13], dissertations [14-19], physics textbooks [20, 21] and journal publications[22-36]

1.1.1 1-D tunneling junction in quantum mechanics

Unlike classical mechanics, in the quantum case, regardless of the fact that the energy of the particle is lower than the energy barrier, there is still a possibility that the particle can tunnel through the barrier. In the simplest one dimensional (1-D) case, as showing in Fig 1.1, there is an idealized energy barrier of height U_0 and width d. In quantum mechanics, for a particle whose energy E is smaller than U_0, its wave function must satisfy the Schrodinger equation,

$$\Big(-\frac{\hbar^2}{2m}\frac{d^2}{dx^2}+U(x)\Big)\psi(x)=E\psi(x) \tag{1.1}$$

The incident wave function to the left of the barrier is a sinusoidal oscillation with amplitude of A_{in}. By solving Equation (1.1), in the barrier region, the amplitude of the wave function is the decaying exponential,

$$\psi(0\leq x\leq d)=\psi(0)e^{-x/\eta}=A_{in}e^{-x/\eta} \tag{1.2}$$

where $\psi(0)=A_{in}$. The penetration distance η is given by

$$\eta=\frac{\hbar}{\sqrt{2m(U_0-E)}} \tag{1.3}$$

The wave function decays exponentially in the region of barrier, but before it decreases to zero, it already reaches the right edge ($x\leq d$), where again the exit wave function behaves as an oscillation with amplitude

$$A_{ex} = \psi(d) = A_{in}e^{-d/\eta} \tag{1.4}$$

Since the probability of finding a particle in location x is proportional to $|\psi(x)|^2$, the probability that the particle tunneling through the energy barrier U_0 from left to right is:

$$P_{tunnel} = \frac{|\psi(x)|^2_{ex}}{|\psi(x)|^2_{in}} = \frac{|A_{ex}|^2}{|A_{in}|^2} = \left(e^{-d/\eta}\right)^2 = e^{-2d/\eta} \tag{1.5}$$

As shown here, the particle has a chance to tunnel through the energy barrier, despite the fact that its energy is lower than the barrier.

1.1.2 Theoretical model of tunneling current

Similar to the 1-D quantum tunneling model, in STM, electrons of a metallic sharp tip and a conducting sample are also competent to tunnel through the tiny gap in the range of several Angstroms. As shown in Fig 1.2, when the metallic tip is scanning on a conducting sample with a few Angstrom distance and a bias voltage V_0, a tunneling current can be generated by the overlap of the tip and sample wave functions. From Equations 1.3 and 1.5, in the simplest 1-D model, the factor of $e^{-2d/\eta} = e^{\frac{-2d}{\sqrt{2m_e(U_0-E)}}}$ dominates the probability that an electron on the tip or sample can tunnel through the gap and engender the tunneling current. It emerges that the exponential decay depends on the width of the gap d and the square root of barrier height U_0. With the mass of electron m_e, normal barrier energy between tip and sample, and Plank constant $\hbar$, it gives a good approximate estimation, that the tunneling current decreases an order of magnitude as the distance increases one Angstrom. Compared with optical microscopy or electromagnetic wave microscopy (X-Ray,

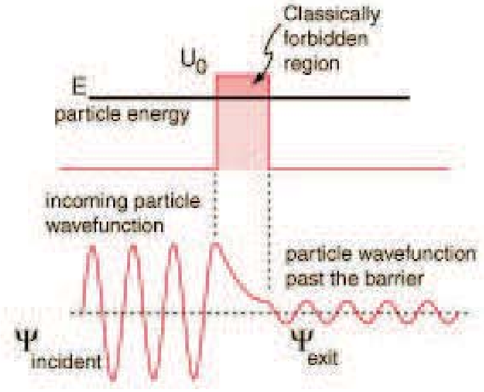

Figure 1.1: Tunneling through an idealized energy barrier.[13]

e-beam), STM makes a dramatic improvement in spatial resolution. When Gerd Binning and Heinrich Rohrer invented the STM in 1982, it was the first time that scientists could get a clear atomic-scale image [22].

However, the real STM is much more complex than this 1-D quantum tunneling model. In order to explain the electron tunneling between a weakly coupled tip and sample, using first order time-independent perturbation theory [37], the tunneling current I can be evaluated as,

$$I = \frac{4\pi e}{\hbar} \int_{-\infty}^{+\infty} [f(E_f - eV + \epsilon) - f(E_f + \epsilon)] \times \rho_t(E_f - eV + \epsilon)\rho_s(E_f + \epsilon)|M|^2 d\epsilon \qquad (1.6)$$

where $f(x)$ is the Fermi distribution function; ρ_t and ρ_s are the electron density of states of the tip and the sample, respectively; $|M|^2$ is the tunneling matrix element showing betweenbv the modified wave-functions of the tip and the sample. For 0K temperature approximation (our research interest is at 85K or around 14K, which is proper to use this

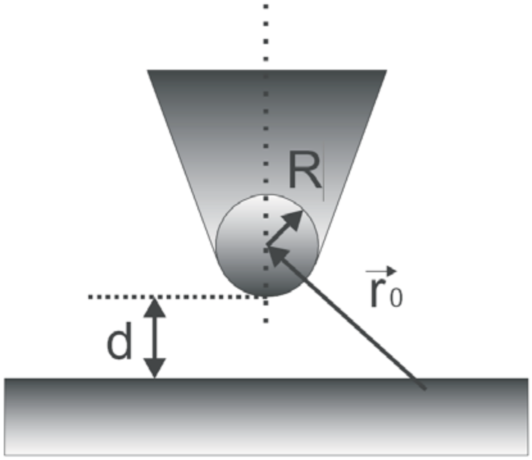

Figure 1.2: Schematic diagram of the tunneling configuration of a Tersoff-Hamann model: d represents the tip-sample distance, R the effective tip radius, and $\vec{r_0}$ the vector from the sample region to the center of the tip.

approximation), the $f(x)$ can be approximated as a step function,

$$f(E) = \begin{cases} 1 & \text{where } E > E_f \\ 0 & \text{where } E < E_f \end{cases} \tag{1.7}$$

which makes Equation 1.6 become,

$$I = \frac{4\pi e}{\hbar} \int_0^{eV} \rho_t(E_f - eV + \epsilon)\rho_s(E_f + \epsilon)|M|^2 d\epsilon \tag{1.8}$$

Including the geometry of the tip and the shape of wave function into Equation 1.8, Tersoff and Hamann built a model which can approximately describe the tunneling process in STM configuration [38, 116]. As shown in Fig. 1.2, they describe an ideal tip as a single sphere atom (in our system this atom is made by tungsten), and only the s-type wave function contributes to the tunneling matrix element $|M|^2$. Thus, as in our STM, an ideal tungsten tip has a flat density of states near the Fermi level, and also the variation of tunneling matrix elements $|M|^2$ is so small in the bias voltage range that it can be replaced by a constant factor. Then, Equation 1.8 becomes,

$$I = \frac{4\pi e}{\hbar}\rho_t(E_f)|M|^2 \int_0^{eV} \rho_s(E_f + \epsilon)d\epsilon \tag{1.9}$$

Including the geometry between tip and sample, the density of states of the sample $\rho_s(E_f+\epsilon)$ is a function of both the Fermi energy of the sample and also the location $\vec{r_0}$. So finally, the tunneling current equation is,

$$I = \frac{4\pi e}{\hbar}\rho_t(E_f)|M|^2 \int_0^{eV} \rho_s(E_f + \epsilon, \vec{r_0})d\epsilon \tag{1.10}$$

1.2 Experimental Setup

All the experimental data are recorded by a continuous flow cryostat STM, as shown in Fig 1.3 A). With a full 60L liquid nitrogen(LN_2) dewar, the system has the ability to image up to six days at a temperature of 85K, and four days for a regular 100L liquid helium(LHe) dewar at a temperature of 14K. By controlling the flow of cryogenic liquid, the system can be efficiently controlled under any temperature above the lowest limitation. The ultrahigh vacuum (UHV) chamber also combines with a mass-spectrometer, which is used to check the purity of the molecular sample, and to do temperature programmable desorption (TPD). A sputter gun assisted with an anneal filament and a leak valve, produce sputter-anneal cycles which are used to clean the Cu(111) surface. A small preparation chamber separated by a gate valve is utilized to clean, bake and degas the Bi_2Se_3 crystal substrate and other solid or liquid status molecular samples before transferring or dosing them to the main chamber.

1.3 Substrate and sample preparation

Except for the Bi_2Se_3 crystal, all the other studies in this dissertation use Cu(111) single crystal as substrate, as shown in Fig 1.3 B), which has a face centered cubic unit cell with a lattice constant of 2.55 Å. For the sample preparing process, first, UHV chamber is backfilled with ultra-high purity (99.999%) Ar gas to 10^{-5} torr. Using the ion sputtering gun with a 3KV electronic field, the Ar^+ ions are produced and accelerated to hit the sample, which ablate the copper crystal surface with their high translational energy. After 20 minutes of sputtering, the combination of turbo and rotary pumps pump back the UHV chamber to 10^{-10} torr, so the sample is kept in clean condition. Then, nearly 30w DC power goes through the tungsten annealing filament underneath the sample, which helps to heat the copper sample to above 600K. It takes 20 minutes to keep annealing the sample, followed by cooling down the sample to room temperature. Normally, after six to eight of these sputter-anneal cycles, the cleanliness of the copper sample is immediately examined under room temperature. Then, liquid nitrogen is used to cool down the copper crystal to 85K. Then, the copper substrate is re-imaged again to make sure it is clean enough under low temperature, and ready for dosing the sample molecule.

For Bi_2Se_3 crystal, as shown in Fig 1.3 C), a triangular molybdenum plate is stabilized on the middle of the ramp by three pairs of screws and nets, where Bi_2Se_3 crystal is glued and conducted by silver paste (Epoxy Technology $H21D$). On top of the crystal, a short and thin rib, which is used to cleave the sample, is glued by non-conducting glue. Then, the whole ramp is kept inside a small preparing chamber, which is baked overnight at approximately 80°C, before moving into the UHV chamber and directly cooling down to

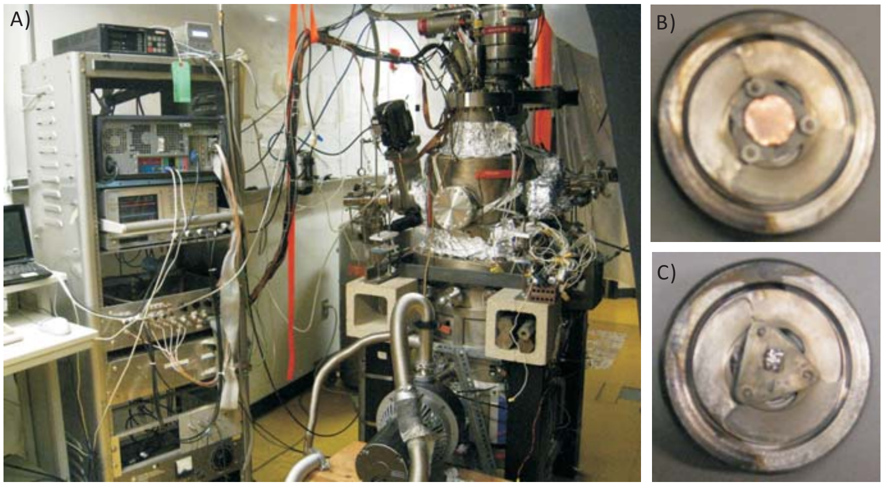

Figure 1.3: Pictures of STM, Cu(111) substrate and Bi_2Se_3 substrate.A) Continues flow STM with LN_2 dewar and electronic control system. B) Ramp with Cu(111) substrate in the center. C) Ramp with Bi_2Se_3 substrate in the center.

85K by liquid nitrogen. The crystal is cleaved in the UHV chamber at 85K and immediately checked for proper thickness by directly procuring to tunneling distance.

Based on different states of molecular sample, there are two distinct dose methods. For gas molecules, since most of the commercial gas has high purity, it can be directly deposited to the copper substrate, after baking the gas line for over two hours and two or three flush cycles, by installing a leak valve between the UHV chamber and the gas cylinder in order to control the amount. For liquid or solid status molecules, they are kept in glass tube, from which the status of the sample is visible through the glass. If necessary, before heating and dosing the sample molecule to the clean substrate, several freeze-pump-thaw cycles are needed in order to degas and increase the purity. Likewise for the sample whose vapor pressure is too high at room temperature (or melting point is too low), a leak valve is still needed to control the deposit amount.

1.4 Theoretical simulation (DFT calculation)

As described before, the tunneling current is not just a function of the topographic features of the sample surface, but also affected by the electronic properties of both tip and sample. So theoretical simulation is always helpful to separate these two distinctive contributions, in order to understand and interpret the experimental data, and analyze more detailed information for the substrate and molecular system. In our lab, we use density functional theory (DFT) to simulate the STM image. Most of these works are done by graduate student Jonathan Wyrick, Chen Wang, and undergraduate student Connor Holzke, Daniel Salib, and Eric Chu. DFT calculations use the VASP code[13-16] with the Generalized Gradient Approximation (PBE-GGA) approximation[17, 18] for the exchange-correlation functional and a projector-augmented-wave (PAW) basis[19, 20]. All results are optimized so that the remaining forces are less than $0.03eV/\text{Å}$.

1.5 Following chapters at a glance

Chapter 2 is mainly focused on the electronic control system about the STM. After introducing the basic design of Besocke scanner and how to use piezo to accomplish coarse approaching, sample manipulation and scanning, I demonstrate my contribution on design and build the electronic control box, as a signal bridge between the computer and the STM. My first research project is assisting Postdoc Zhihai Cheng to studying CO molecules adsorbed into the pores of an organic molecular self-assembled network and confined on a metal surface. We dosed anthraquinone (AQ) molecules on Cu(111) surface and annealed to self-assemble honeycomb structure. And then CO molecules were deposited into the pores of this confinement network. Different CO diffusion rates are observed depend on different CO coverage, as well as the different preferred adsorption sites inside the pores. These result are exhibited inside Chapter 3 and 4.

In chapter 5, it is my first dominant project, that imaging high coverage acetylene molecules on the Cu(111) surface. The molecule has a beautiful long range periodic pattern on the Cu surface. Under conditions in which the STM tip picked up one acetylene molecule, the molecular pattern shows different apparent structures from what actually lies underneath. Using VASP, we theoretically simulated the effect of this picked-up acetylene on the STM tip and how its rearrangement affects imaging.

Chapter 6 shows my work on metal coordination complexes of cyano-naphthalene vs isocyano-naphthalene species with a Cu adatom. By imaging the different coordination patterns under LN2 temperatures using STM and comparing to theoretical calculations of the electron density transformations under these two different species, the result exhibits the difference between various ligands and their electronic contributions to the metal coordinate center.

In Chapter 7, I try to extend my research tools on surface science. I collaborate with graduate student Quan Ma, John Mann and Patrick M Odenthal, using Photoelectron Spectroscopy not STM to characterize the modified band gap shift on monolayer MoS_2. XPS, Raman and PL data are provided.

Chapter 2

Electronic control system

Fig 2.1 is a basic schematic diagram of STM. As shown here, in order to make the tip reach tunneling distance (coarse approach), move along the sample surface to seek a flat area (sample manipulation), and image the topography of the sample (scan), three different mechanisms are required. There are many different types of scanners used for STM based on different mechanisms. In our lab, all three STMs are using Besocke design.

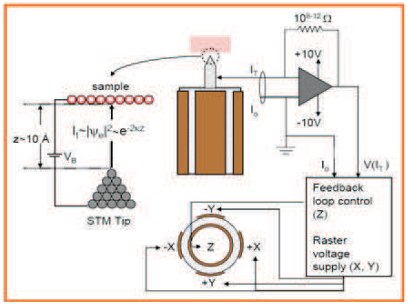

Figure 2.1: Basic schematic diagram of STM

2.1 Besocke type STM scanner design

Our STM scanner is a typical Besocke scanner that consists of three piezoelectric tubes placed in a triangular pattern with a fourth one placed at the center of the triangle. The three outer tubes capped with small metal balls support the sample, which is held down only by gravity, while the center fourth one carries the tip as the scanner.

For *sample manipulation*, as shown in Fig 2.2A, (1) the three outer piezos are moved to the side (X or Y axis) fast enough so that the sample cannot follow because of its inertia. (2) by slowly aligning all three outer piezos back to the vertical position followed by the sample, the sample is shifted.

Fig 2.2C is the schematic drawing of a ramp for the Besocke sample holder. Each of the outer piezo tubes supports the ramp in a 120° zone where the depth changes gradually as shown by the grayness in the figure with a slope of 2°. By sliding down the ramp in a rotational motion, the tip comes close to the sample, which is the process of *coarse approach*.

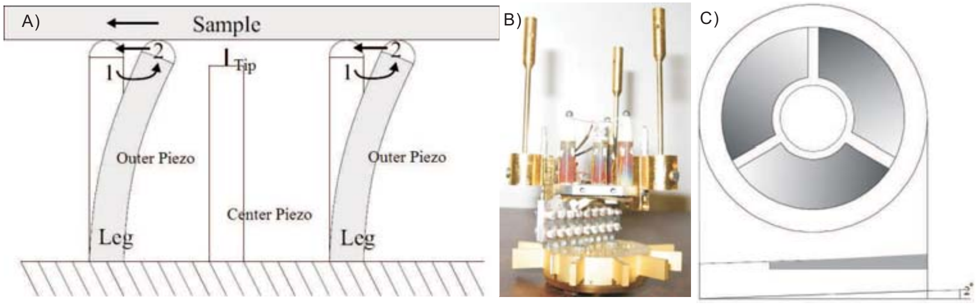

Figure 2.2: A) Schematic drawing of sample manipulation for Besocke scanner. B) Real Besocke STM scanner. C) Schematic drawing of a ramp for Besocke sample holder.

During *scanning*, the three outer piezos slowly move with the sample along the X or Y axis, while the center piezo only moves along the Z axis. Based on distinct responses of the center piezo, there are two different scanning modes, constant high mode vs. constant current mode. If the center piezo keeps the same length (Z axis), and measures the change of the current along the surface, it is in the constant high mode. In the constant current mode, the center piezo keeps adjusting the tip-sample distance in order to keep the tunneling current constant.

Based on the unique mechanisms and purposes of the three outer piezos and center piezo, the electrode configurations for them are slightly different, as shown in Fig 2.3. For the three outer piezos (labeled as A, B, C), there are five signals. Four outside signals (+/- X, +/- Y) are used to control the piezos, so that the sample can move horizontally on X or Y direction (for sample manipulation and scan) or along the rotational direction (for coarse approach). The Z signals (the inner segments) are usually connected to ground (GND) as a reference, but also can be used to move the three outer piezos along the Z axis. The center piezo only needs to move along the Z axis, so the outer four segments are connected to the same signal, in the meantime, the inner segment is connected to GND as a reference. The bias signal is directly connected to the metal balls sitting on top of the three outer piezos, with a piece of ceramic placed between to isolate the signals. On top of the center piezo, there are three layers sandwich stuck structure, where one metal layer sitting inside two ceramic layers. This stuck sit under the tip holder, which connected to tunneling current signal I. The two ceramic layers of the stuck are used to isolate the signals, and the metal film (GND) is a shield between the noisy piezo signals and the tunneling current signal.

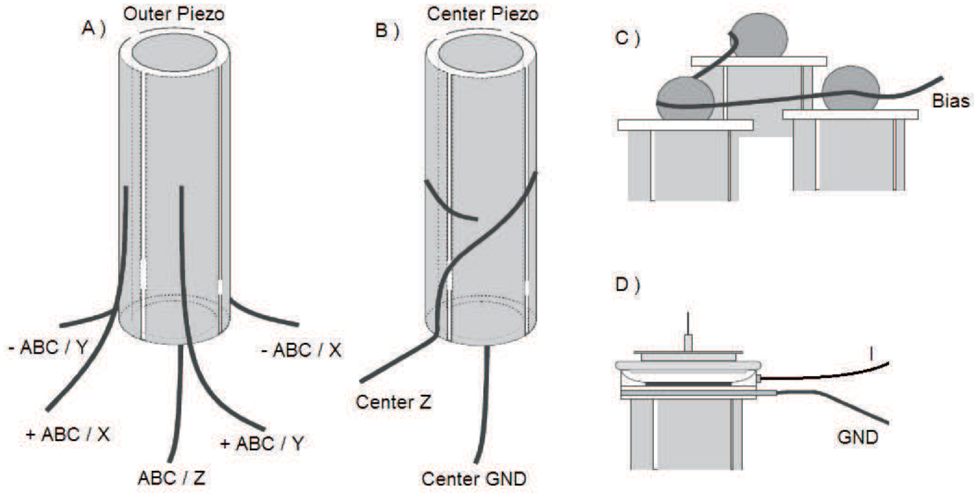

Figure 2.3: Electrode configurations. A) Three outer piezos; B) Center piezo; C) Bias signal; D) *I* current signal & isolation ground.

2.2 Electronic control system

All these electronic signals mentioned above need to communicate with the computer, while the digital signal processor (DSP) is used as a signal convertor (digital to analog or analog to digital) and internal clock. Between the computer (DSP) and the STM, there is a control box used as a filter and an amplifier. The brief schematic diagram is shown in Fig 2.4.

As shown here, there are two different types of electronic signals generated by the computer and sent to the STM. Digital signals, which are used to control the relays in the control box in order to switch between different mechanisms, are promptly sent from the computer through the DSP without any conversion, and are only buffered by the chips inside the control box. Analog signals communicated between the computer and the STM, however, have to be converted by the DSP from analog to digital, or reversed, since the computer

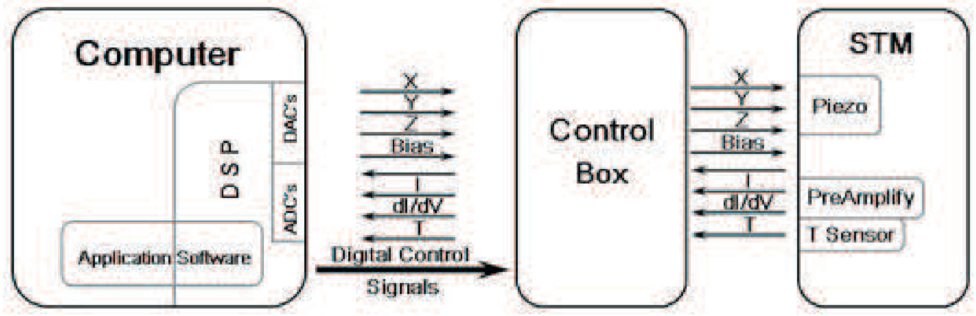

Figure 2.4: Schematic diagram of electronic signal communication.

only accept and work on digital signals. As shown in Fig 2.5, there are four analog signals, which are the bias signal and the X, Y, and Z axis signals for the movement of the four piezos, sent from the computer to the STM. There are also four analog signals sent from the STM to the computer. Two temperature sensors located at the scanner and the inner shell of the cryostat send out local temperatures from the STM to the computer. The tunneling current signal I and tunneling spectrum signal dI/dV are the most important data during the scanning. Beside the DSP, all these analog signals have to be filtered, amplified, and buffered inside the control box, before being sent to the STM or the DSP.

2.3 Control box

My work in the electronic field is mainly focused on designing and building the control box including the printed circuit board (PCB) inside. Besides the front and back panels, the whole control box includes three piezo driver boards, one bias board and one signal board. Their functions are list in the Table 2.1.

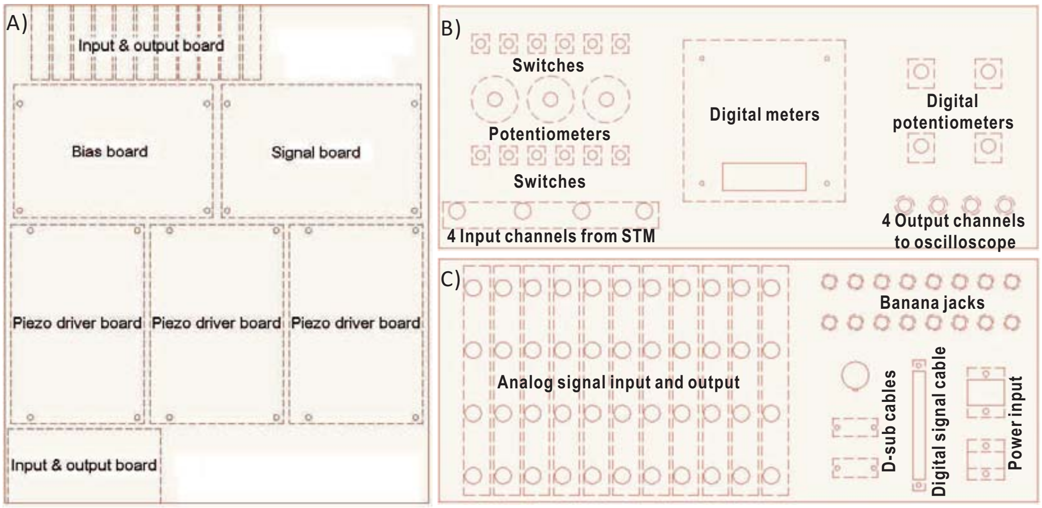

Figure 2.5: Schematic diagram of electronic control box. A) CAD diagram of control box PCB boards layout; B) Front panel layout. 12 switches are used to manually control the relays on each of the boards. Potentiometers send out the shift voltages to search the scanning area on the surface. Three channel digital meters can directly give the reading of selected analog signals. Four digital potentiometers select signals, which are sent to the oscilloscope by four output channels. The only input & output board mounted on the front panel gives four input channels to four analog signals from the STM. C) Back panel layout. Two power input cables are distributed to low voltage power (5V and +/- 15V) and high voltage power (+/- 200V). 11 input & output boards are the channels for all the analog signals sent to the STM. A 40 pin d-sub cable is the bridge between the DSP and the digital signal buffers on the signal board. All the banana jacks are the backup for testing the signals.

Board	Function
Piezo driver boards	Signal board & amplify and filter the analog signals for the X, Y, and Z directions
Bias board	filter the analog signals for the bias signal V, the tunneling current signal I, the tunneling spectrum signal dI/dV, and two temperature signals
Signal board	digital signal buffers, four analog signal selection channels to oscilloscope, and heating current output to sample holder

Table 2.1: Functionalities of five PCB boards inside the control box

2.3.1 Piezo driver board (X axis as an example)

The analog signals used to drive the three outer piezos and the inner piezo come from two different sources. One is from the computer via DSP, and the other is from the potentiometers on the front panel. Both of these two analog signals in the range of -15V to +15V need to be filtered in the low voltage (LV) module and then combined together (if necessary) to be amplified in the high voltage (HV) module.

After being filtered by the instrumentation amplifier (*AMP02*), the voltage difference between the incoming analog signal and ground is sent to four channels operational amplifier (op-amp) (*OPA4227*), that two of these channels are used as a gain $G = -1$, cut-off frequency $f_c = 1/RC = 100KHz$ active low pass filters[39], and the other two are an op-amp based unity gain buffer[40]. Based on the different incoming sources and the different functionalities, four pairs of the low voltage output signals are generated, *XL+/-, Ramp+/-, Compoff+/-, and Manoff+/-*. There are no filters for the *Ramp+/-* signals, since they are only used for course approach, no high accuracy requirement.

- *XL+/-*, scan signal and coarse sample manipulation signal during approach
- *Ramp+/-*, coarse approach signal
- *Compoff+/-*, computer controlled sample manipulation signal during scan
- *Manoff+/-*, manually controlled sample manipulation signal during scan

Two pieces of very high speed (1000V/s) and high voltage (450V) power amplifier (*PA85*) are used to amplify the low voltage signal (-15V to +15V) to medial voltage (MV) range (4:1

ratio) or high voltage range (20:1 ratio), which is controlled by the digital signal *MVSwitch*, acting on *Relay 40*.

Here, digital signal *RampScanControl* acting on *Relay 41* is used to select which pair of low voltage signals are sent to high voltage op-amp as *HV In*. And the Offset signal is selected from two offset sources, *Compoff* and *Manoff* by another digital signal *WhichOffsetSwitch*, acting on *Relay20*.

HV and LV signals are selected as X channel output by digital signal *LVHVSwitch*, acting on *Relay 80* afterward.

2.3.2 Signal board

In digital signal buffer module, 16 pieces of dual pole OptoMOS relay chips (*PAA150*) offer 32 digital signal buffers to accept the digital control signals coming from computer, and then afterward distribute them to all the other boards to switch on/off the relays there. All the digital signals go through integrated drive electronics (IDE) interface for in & out.

There are more than thirty signals communicating between STM and computers. In order to maintain and test the STM, it is important to be able to trace all these analog. In our lab, we use four channels oscilloscope to trace the analog signal. So in analog signal selection

Stutas	Input signals	Ratio	Functionality
On	HV In and Offset	4:1	Scan
Off	HV In	20:1	Coarse sample manipulation and coarse approach

Table 2.2: Functionality of Relay 40.

Stutas	Input signals	Functionality
On	*XL*	Coarse sample manipulation and scan
Off	*Ramp*	Coarse approach

Table 2.3: Functionality of Relay 41.

module, four chips of 16-Channel Analog Multiplexer (*ADG507A*) are utilized to select one signal from 16 signals, based on the digital selection signal from four digital potentiometers on front panel, and send to oscilloscope. All these four output trace signals are buffered by a four channel op-amp (*OPA4227*) chip.

Since the heat transfer inside UHV chamber is really difficult, in order to anneal the sample more efficiently, we put an annealing filament at the backside of sample holder. Heating current output module is designed to give the power supply to this filament.

2.3.3 Bias board

Similarly as all the other analog signals, all the four input analog signals (I, dI/dV, and two temperature signals) and two bias output signals (*Bias-in*, and *Modulation-in*) are filtered by the instrumentation amplifiers (*AMP02*), and afterwards pass through four channels op-amps (*OPA4227*) as active low-pass filters and op-amp based unity gain buffers. Modulation-in signals is controlled by digital signal *BiasModSwitch* activing on *Relay 3* to combine with *Bias-in* signal as dI/dV input to STM.

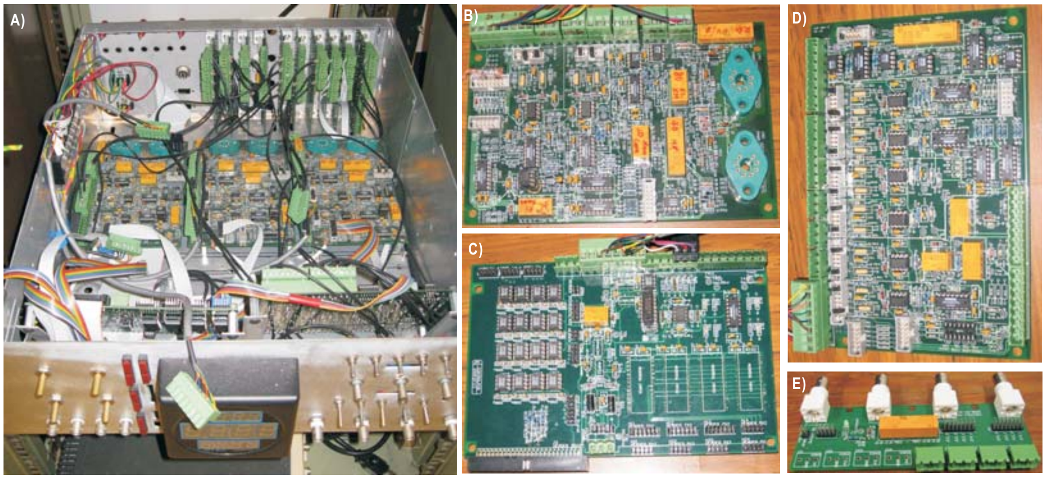

Figure 2.6: A) unfinished Control box; B) Piezo driver board; C) Signal Board; D) Bias board; E) Input & output board.

2.3.4 Input & output board

All these analog signals go through the input & output board with Bayonet Neill-Concelman (BNC) connectors to communicate between the computer to the control box, the control box to the STM, and the control box to the oscilloscope. When the input & output board is used as input to the control box, the analog signals come through the BNC cables to the 3-position terminal blocks *J21, J22, J23, J24*. When the input & output board is used as output from the control box, the analog signals come through the terminal blocks *J11, J12, J13, J14* to the BNC cables, and *Jumper JP1H, JP2H* and *Relay U1* work together to assemble a group of four signals for output.

Chapter 3

Power of Confinement: CO Molecules inside an Anthraquinone Honeycomb Network on Cu(111) Surface – Low Coverage

This chapter is taken from one article I published on *Nano Letters, 10, 1022018 (2010).* Together with the next chapter, this is the first research project I join in, while Postdoc Zhihai Chen is the major contributor to this project. The object for this research time is to see the behavior of small molecules inside a self-assembled organic network. In this project, I helped to acquire the image data using STM and analyze the data using software IDL. This is also the first time I work on STM. In this chapter, the content mainly focus on the low coverage CO molecules behavior inside an anthraquinone honeycomb network on Cu(111) surface.

3.1 Introduction

Understanding the adsorption of molecular species at solid surfaces resonates as one of the unifying themes throughout the evolution of surface science over the past half-century. The adsorption of an ever-increasing number of molecules on crystallographic surfaces, as well as on steps and at other defect sites, has been studied. Great progress has been made in the development of computational techniques that reveal the electronic interaction between adsorbates and the underlying substrate atoms. However, the effect of lateral confinement of the support on the nanometer scale has remained largely unaddressed because of challenges in the preparation of surfaces covered with atomically identical patterns several nanometers in scale and because of computational limitations in simulating systems consisting of many hundreds of substrate and adsorbate atoms. Yet many of the applications of surface science, for instance in heterogeneous catalysis or in semiconductor processing, crucially rely on nanoscale-delimited surfaces; and recent progress in these fields emphasizes the effects of nanoscale confinement [41] and diminishing scale, respectively.
In this Letter, we address how confinement of the substrate to approximately 4 nm hexagons [42]i.e., larger than most adsorbate patterns [43-45] and substrate unit cells but smaller than previously investigated structures such as quantum corrals and adislands [46,47]affects the distribution and energetics of small molecule adsorption. A number of molecular surface networks, including hydrogen bonded [48] and boron-nitride ones [45,49], have been shown

to template adsorption of subsequent species [44].

It has been shown that perturbation of substrate electronic states, such as an underlying gas bubble [50] or scattering of a Shockley surface state at a step edge [51] or adatom row [52], affects the distribution of adsorbates. Substrate-mediated long range interactions between molecules have been found in a variety of systems and quantified in a number of cases by scanning tunneling microscopy (STM) [42,53-63] and field ion microscopy [64-66]. A correlation between the location of CO molecules on Ag(111) [67] and benzene on Cu(111) [51], with the phases of the surface scattering amplitude, has been proposed from experimental data and through theoretical modeling [28,29]. In this experimental study we show that confined electronic states of the substrate can actually be titrated with adsorbates, arguably much as electronic states are filled up from the lowest to highest energy in an atomic orbital diagram.

3.2 Experiment Setup

Our measurements were conducted on a Cu(111) surface decorated with a chiral anthraquinone (AQ) network of sixfold symmetry (disregarding the substrate) exhibiting pores that expose 186 substrate atoms in their midst [42] [Fig. 1(a)]. We use CO as our test molecule because a wealth of data on its surface behavior is available: CO molecules adsorb upright atop Cu(111) substrate atoms. They are imaged in STM as protrusions or indentations, depending on whether the STM tip is decorated with a CO atom at its apex or not, respectively [70].

Sample preparation involves the usual sequence of sputtering and annealing, followed by cooling to liquid nitrogen temperatures. The AQ pattern is created by evaporation of the molecule onto the cryogenic sample followed by annealing to room temperature. Deposition of CO molecules through a leak valve onto the AQpatterned surface at 40 K preserves the pore shapes.

3.3 Result and Analysis

We find that the AQ network blocks the diffusion of adsorbed CO molecules on the substrate; repeated imaging of the same set of pores allows tracking of the perambulation of a fixed number of molecular entities within a confined area. Figures 1(b) and 1(c) show images from a movie [71] of a set of pores, in each of which a few molecules are seen to diffuse. In such sequences of images each molecule can be assigned to a particular substrate atom on which it is adsorbed. From thousands of images obtained, we calculate histograms of the occupation of the various substrate sites within the confined area [Figs. 2(a) 2(e)]. Each confined area consists of 62 threefolddegenerate (186 in total) adsites surrounding a hollow site at the pore center in a threefold symmetric arrangement. The AQ network is chiral, removing inversion symmetry.

The radial distribution of CO molecules in pores of different coverages is shown in Fig. 3(a). Given the large number of different adsites, we construct seven radial bins, as indicated in the inset of Fig. 3(a). In pores containing a single CO molecule, the CO is generally found at the pore center; in 54% of the cases, the molecule occupies one of the two inner bins of Fig. 3(a). From the distribution of Fig. 2(a), we can obtain the radial variation of the probability P_i of CO occupation of an adsite i indicated in the yellow (front) curve of Fig.

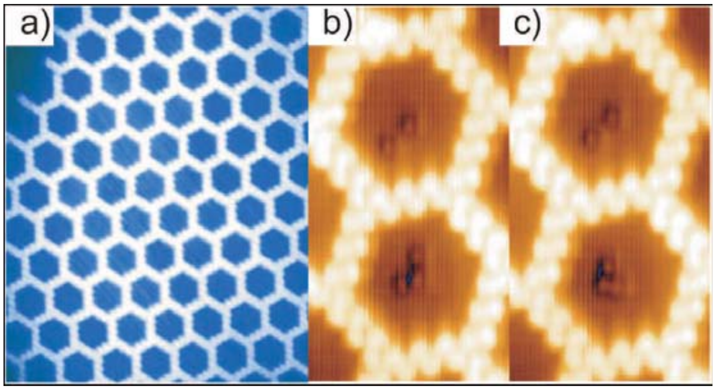

Figure 3.1: (color online). (a) An array of atomically defined pores on Cu(111) formed by deposition of anthraquinone according to Ref. [42] Image parameters: 38 nm × 43 nm; Bias: -2.534 V; Current: 50 pA. (b, c) Images from a movie showing the diffusion of two and three CO molecules in confinement. Image parameters: 6 nm *times* 10 nm; Bias: -2:673 V; Current: 99 pA.

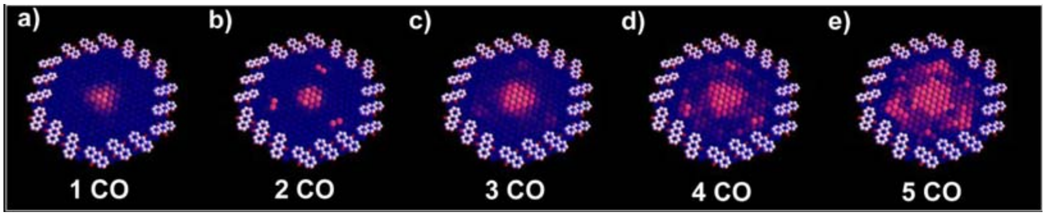

Figure 3.2: (color online). Color-coded plots of the probability of CO molecule occupation for each of the 186 Cu substrate atoms exposed within an AQ pore. Each plot is based on > 500 CO configurations observed and averaged over equivalent locations.

3(a). From this data set we can construct the canonical partition function Z of the single CO system, which allows us to deduce the radial variation of the CO adsorption energy ε [Fig. 3(b)].

$$Z = \sum_i e^{-\varepsilon_i/kT} with P_i = e^{-\varepsilon_i/kT}/Z \tag{3.1}$$

with k the Boltzmann constant and T the temperature 27 K of our measurements. The resultant variation of $\approx$ 14 meV is quite substantial, approximately 1/5 of the CO/Cu(111) diffusion barrier of 75 meV [56].

For two CO molecules in the system [Fig. 2(b)], we find generally that either both molecules occupy the confinement center or they are split between the center sites and a set of three equivalent adsites approximately halfway towards one set of confinement vertices. The same set of three adsites is also favored in pores that contain 35 molecules [Figs. 2(c)2(e)]. Experimentally, these are independent data sets acquired on different pores, days, and sample preparations; the reappearance of the same location for pores of different coverage rules out experimental error (e.g., through subsurface defects) as the origin of the peripheral peaks in Fig. 2. This poses the question of their physical origin and, in particular, the reason for their threefold symmetry. The $\approx$ 4 nmdiameter of the pore rules out direct intermolecular interactions, suggesting that a substrate-mediated effect may be of relevance. Unfortunately, first-principles computational methods (such as density functional theory) are incapable of treating a system that requires at least 186 substrate atoms per layer (i.e., several hundred in total).

Prompted by the idea that surface states get reconstituted in laterally confined geometries [43,46,72], we turn here to a much simpler continuum model of the surface-bound states

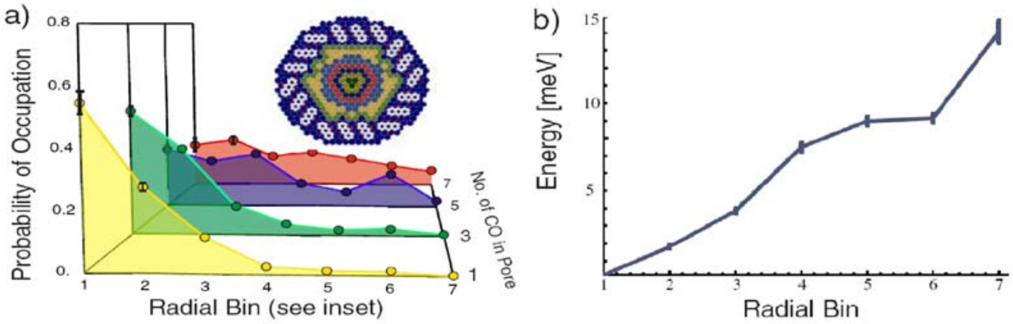

Figure 3.3: (color online). (a) Normalized probability of occupation of radial bins (shown in the inset, normalized to the number of substrate sites they encompass) for pores containing 17 molecules. For 1,3 molecules, the distribution is monotonic, whereas at increasing number of molecules, an additional intermediate distance also becomes favored until further increase of the coverage renders the plot featureless. (b) Variation of the adsorption energy of a single CO molecule across a pore. Error bars are based on $\sqrt{counts}$ in the histogram and are shown in panels (a, b) when larger than the data markers.

derived from the Cu(111) surface state. In this context it is important to realize that although the pore boundary itself is sixfold symmetric, the pore vertices are alternatingly centered on hcp and fcc hollow sites, so that the overall symmetry of the pore on the substrate has the same threefold (and not sixfold) symmetry as the CO distribution [Fig. 2]. Thus, we calculate the confined electronic states within the pore starting from the known solutions of a particle in a triangular box [73], followed by relaxation into the actual geometry of the pore.

Gross et al. showed that scattering of the surface state from organic molecules occurs not at the peripheral hydrogen atoms but at the 2nd period elements [74]. Hence, we construct the boundary of our pore from the six carbon and oxygen atoms per molecule (102 in total) that are closest to the pore center. We adapt an iterative finite-difference algorithm [75], more commonly used for solution of Poisson or heat-diffusion equations, to the relaxation of the known solutions into the geometry of the pore. Here, we develop the wave function in a Taylor series to third order; summing over four locations adjacent to a point (x, y) reproduces the Hamiltonian Hinside inside the potentialfree pore.

$$\frac{\langle x+\delta,y|+\langle x-\delta,y|+\langle x,y+\delta|+\langle x,y-\delta|}{\delta^2}|\varphi\rangle-\frac{4\langle x,y|\varphi\rangle}{\delta^2}\cong\langle x,y|\frac{-2m^*}{\hbar^2}H_{inside}|\varphi\rangle=\langle x,y|\frac{-2m^*}{\hbar^2}E|\varphi\rangle \tag{3.2}$$

with m^* the effective mass of an electron of the surface state of 0.34 electron masses and δ a small displacement. Thus, if φ_{n-1} is an approximate eigenfunction of the Hamiltonian, a better approximation φ_n can be found by evaluating

$$\langle x,y|\varphi_n\rangle=\frac{\langle x+\delta,y|+\langle x-\delta,y|+\langle x,y+\delta|+\langle x,y-\delta|}{4-2m^*\delta^2E_{n-1}/\hbar^2}|\varphi_{n-1}\rangle \tag{3.3}$$

Alternating this iteration and Gram-Schmidt orthogonalization [76] of the set of eigenfunctions originally obtained from the triangular particle in the box problem, we end up with three eigenfunctions (one unique and one twofolddegenerate) whose eigenvalues E of 170 meV and 440 meV, respectively, are below the Fermi energy E_F, if measured from the bottom of the surface state band of 450 meV below E_F [72,77]. Figures 4(a) and 4(b) show the distribution of local density of state (DOS) associated with the first and twofold-degenerate second state, respectively. Our algorithm provides correct eigenfunctions and eigenstates that are converged and invariant to the grid spacing δ of $1.25\mathring{A}$, $0.63\mathring{A}$, or $0.41\mathring{A}$ (corresponding to using a 40×40, 80×80, or 120×120 points grid to represent the pore); however, it cannot guarantee completeness of the set of eigenfunctions and eigenvalues found. Summation of the fraction of the surface Brillouin zone filled by the surface state (characterized by the Fermi vector $k_F=0.21\mathring{A}^{-1}$) [77,78] over the exposed substrate atoms leads to no more than three complete electron pairs in the surface state within each pore, in good agreement with the three states found. This result is further corroborated by the recent finding of Lobo-Checa et al. by electron spectroscopy that in a molecular surface network of roughly 1=3 the size of our system, there is exactly one confined state [43].

Comparison between the DOS of Fig. 4 and the molecular distribution within the pore of Fig. 2 shows that CO molecules preferentially occupy locations in the pore that feature a high DOS of the confined surface state, supporting a picture that adsorption energy increases with DOS. Moreover, we find that if only one molecule occupies the pore, it seeks out preferentially the pore center where the lowest-energy confined surface state is located. Increasing the coverage leads to occupation of locations corresponding to the more energetic second confined state. Thus, increase of the CO coverage may be likened to the "titration" of the locations inside the pore that show appreciable local DOS of the confined surface state. The fact that the sequence in which these locations are occupied matches the energetic succession of the corresponding confined surface states reminds one of the filling of electrons into an atomic orbital diagram.

Previous modeling of surface-state-mediated interaction of adsorbates has generally employed a scattering-based formalism related to the modeling of the lateral surface state distribution at E_F visible in STM. This has been shown to work well for systems that involve no confinement of the surface or dimensions much longer than the surface state Fermi wavelength [58,68]. The energy integrated approach described here is more suitable to the relatively small scale of pores in molecular surface networks where the confinement size does not exceed the Fermi wavelength by much. Fiete and Heller showed that for circular

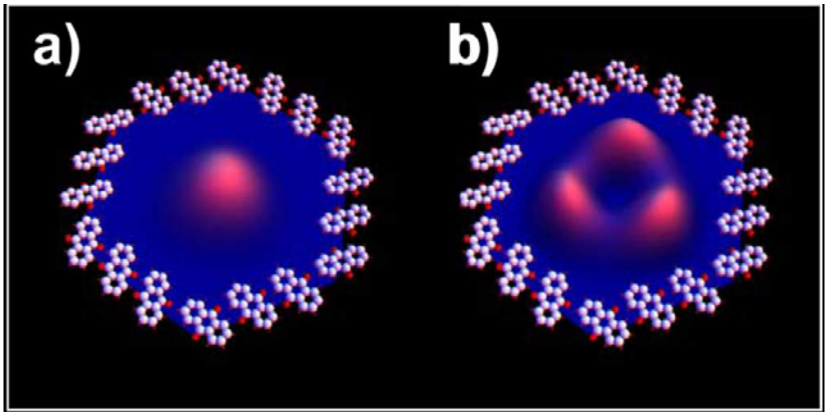

Figure 3.4: (color online). Plots of the local DOS of (a) the lowestenergy electronic state of the pore and (b) superposition of the two degenerate second electronic states of the pore. Compare to the distribution of molecules in pores in Fig. 2.

quantum corrals at larger corral size, both approaches lead to equivalent results for the energyresolved surface-state local DOS [72]. Increasing the number of molecules inside the pore beyond the number of electrons in the surface state (i.e., six) causes the radial distribution of molecules in the pore to become more uniform [red curve in Fig. 3(a)], showing the limitation in adsorbate guidance achievable in a pore of given size. This finding corresponds with COs ability to quench the surface state at relatively low coverage.

3.4 Conclustion

Although our calculations were based on free-electronlike behavior of the surface state electrons (i.e., a constant potential within the pore boundary) with just an effective mass accounting for the presence of the substrate, our finding of threefold symmetry (as enforced by the substrate, in contrast to the sixfold symmetry of the molecular network) is crucial for explaining the experimental distribution of adsorbates; this highlights the limitation of the free electron approximation in understanding surface state electrons and their impact on adsorption. In summary, by monitoring adsorbate diffusion within a nanometer-scale confined system we found that such confinement has a pronounced effect on their average location, suggesting that engineering of confinement boundaries may not only allow engineering of surface electronic states but can also be a tool in assembling molecular patterns at surfaces.

Chapter 4

Power of Confinement: CO Molecules inside an Anthraquinone Honeycomb Network on Cu(111) Surface – High Coverage

This chapter is taken from one article I published on *Physical Review Letters, 105, 066104 (2010)*, which comes from the same research project as Chapter 3, but on different emphasis. In this chapter, the content mainly focus on the high coverage CO molecules behavior inside an anthraquinone honeycomb network on Cu(111) surface.

4.1 Introduction

The diffusive behavior of adsorbates has generally been studied on extended terraces, that is, not under lateral confinement, mainly due to experimental impediments, yet metal clusters with nanoscopic facets have considerable technological relevance, for instance as supported metal catalysts for applications ranging from the (petro-)chemical industry to emission control. For the study of the dynamics of adsorbates on nanoscale clusters, it would be ideal if arrays of atomically identical ones could be formed. Absent this possibility we utilize a Cu(111) substrate covered with a self-assembled anthraquinone network. This network sustains subsequent deposition of CO molecules and confines their diffusion into pores of ∼4 nm in size, where they can be imaged and studied in detail.

The pores have a similar size as the facets expected on catalytic nanoclusters; in particular, studies on gold have shown that its activity increases enormously if dispersed in this size regime.[79,80] Conventionally, the high activity of nanoparticles, as compared to the surfaces of bulk metals, is attributed partly to the high surface to volume ratio at high dispersion, and partly to support-metal interactions and to the abundance of surface defect sites such as step-/facetedges and -kinks.[81] While the exposed copper facets of our network probably have little besides their size in common with catalytic nanoparticles, they nevertheless open for study the kind of effects that lateral confinement may have on the dynamics of adsorbates, at least in a phenomenological manner; a survey of them is the objective of this study.

Several previous publications addressed the dynamics of adsorbates at metal surfaces and their interaction with one another. They include measurements of the dynamics of benzene molecules,[82,83] reactive mixtures,[45,46] hydrogen atoms,[86] and CO molecules.[56,57,67,87-89] Also, the insertion of atoms or molecules into molecular surface networks has been studied previously.[44,48,49,90-92] What makes our study novel is the confined nature of the adsorbates that allows us to study how molecules behave when their support is not a large, clean, and inert terrace.[93]

4.2 Experiment Setup

We use CO as our test molecule because abundant data on its surface behavior is available: CO molecules adsorb upright atop Cu(111) substrate atoms. They are imaged in scanning tunneling microscopy (STM) as protrusions or indentations, depending on whether the STM tip is decorated with a CO atom at its apex or not, respectively.[70] At sufficient coverage, CO adsorbates form an ordered $\left(\sqrt{3}\times\sqrt{3}\right)R30^\circ$ overlayer; large islands of this superstructure have been observed in previous STM studies.[94] In our model system there are 186 exposed atop adsites in each 4 nm pore, allowing a maximum occupation in the exposed facet of 62 CO molecules in a dense $\left(\sqrt{3}\times\sqrt{3}\right)R30^\circ$ adlayer.

Initial sample preparation involves the usual sequence of sputtering and annealing, followed by cooling to liquid nitrogen temperatures. The anthraquinone pattern is created by deposition of the molecule onto the cryogenic sample followed by annealing to room temperature. After subsequent cooling to $\sim 40K$, CO is deposited through a leak valve.

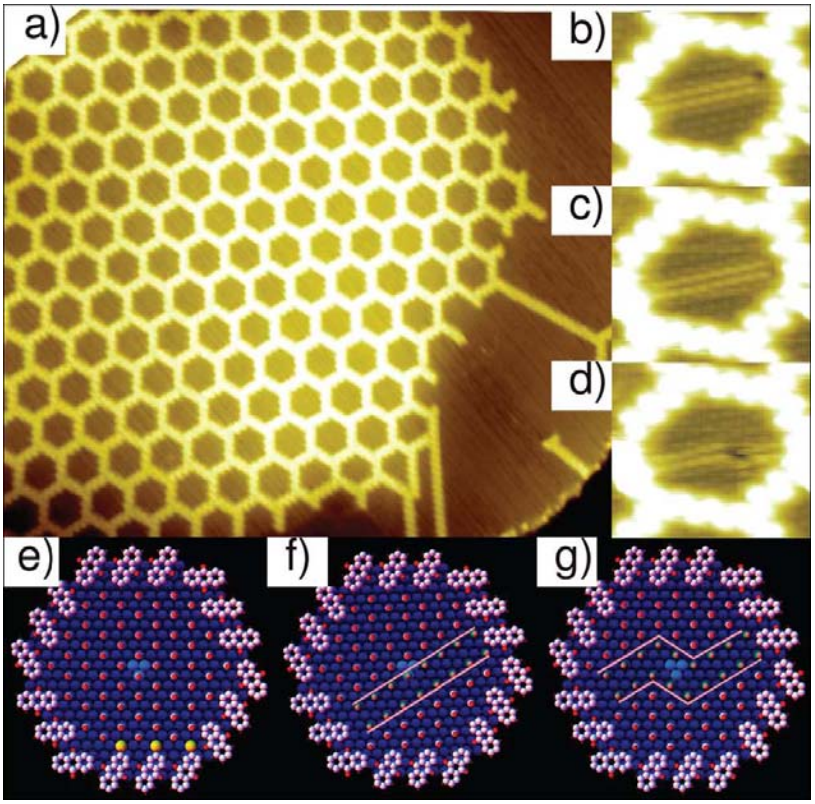

Figure 4.1: (a) Array of atomically defined pores on Cu(111) formed by deposition of anthraquinone according to ref 1. Image parameters, 83 nm × 73 nm; bias, -2.53 V; current, 50 pA; temperature, 90 K. (b-d) Images from a supporting movie of a dislocation line moving in confinement. Image parameters: bias -2.40 V; current 44 pA; temperature, 24 K. e,f) The $\left(\sqrt{3}\times\sqrt{3}\right)R30^{\circ}$ adlayer can be anchored at any one of the three atoms at the center of the exposed facet (light blue). In each case, one facet edge is decorated differently than the remaining two of the same kind (yellow in e). This can be alleviated, if a dislocation line is induced in the pore (f). In both cases, the same number of molecules fit inside the pore. (g) Model of a kink in a dislocation line similar to the STM image of panel d.

4.3 Resulet and Analysis

Deposition of CO molecules into an anthraquinone honeycomb network does not alter the pore shape. With careful dosage we obtain a CO coverage very close to a complete $\left(\sqrt{3} \times \sqrt{3}\right) R30^\circ$ overlayer, which is visible inside the pores (Figure 1b-d). Moreover, we find on the exposed facets a dislocation line, which is constantly present yet persistently shifting position. The Supporting Information shows amovie. This differs from the behavior of CO films on extended terraces, where the $\left(\sqrt{3} \times \sqrt{3}\right) R30^\circ$ is observed over large areas and dislocation lines (i.e., antiphase domain boundaries) are expelled to the edge.[94] What is the origin of this effect?

Each exposed facet is centered around a substrate hollow site, allowing three equivalent atop adsites (light blue in Figure 1e to anchor the CO $\left(\sqrt{3} \times \sqrt{3}\right) R30^\circ$ pattern, thus spanning three equivalent overlayer sublattices. The facet edges consist of two alternating sets of three equivalent sides, much as any hexagonal fcc island is surrounded by steps with alternating (111) and (100) facets. One of the sets of sides is equally decorated with CO molecules no matter which central substrate atom anchors the overlayer. Of the other set of sides, however, only two are covered intimately, leaving open space near the third side (yellow in Figure 1e).

The open space can be avoided if the CO adlayer is imperfect; a dislocation line in the overlayer allows placement of adsorbates at all sides of the second set equivalently. Consequently, the confined adlayer is under competition between forming the structure found on extended surfaces and incorporation of a dislocation line that permits equal filling of the edge sites, that is, providing optimal edge interaction at the expense of intermolecular interaction. In both cases, the same number of CO molecules fit onto the exposed facet. The observation of the persistence of the dislocation lines indicates that the interactions at the adlayer edge are dominant over those within the adlayer.

Imaging 75 setups of one dislocation line at 24 K, we find that in $\sim 40\%$ of the cases a kink is present in the line. A dislocation typically affects 16 molecules (8 per side); a kink in the double line increases this number by 2 along the dislocation line (Figure 1g). Analyzing the measured fraction of kinked lines using the Boltzmann equation and taking into account the degeneracy of the various possible kinked configurations, we estimate a kink energy of 6.1 ± 0.3 meV and a total energetic cost of the entire dislocation line of 0.05 eV. For three molecules, the edge-interaction is improved by the dislocation line (yellow in Figure 1e). This yields a lower boundary of the edge interaction of 0.02 eV per molecule, a considerable energy compared to, for example, the CO diffusion barrier of 0.075 eV.[56]

The presence of the dislocation can potentially affect the chemical reactivity of the film markedly; molecules affected by a dislocation line have a nearest neighbor configuration that allows more ready access to them as well as the underlying substrate. The number of molecules affected by the dislocation scales linearly with the size of the facet, whereas the total number of molecules scales quadratically, indicating that the smaller the facet size, the more pronounced this effect. For the 4 nm facets studied here, more than one-fourth of the adsorbates (16 out of 62) are directly affected by the dislocation line, significantly greater than on extended terraces.

The constant motion of the dislocation lines well below 30 K contrasts substantially with the behavior of individual CO molecules on Cu(111), whose diffusion starts only at ~ 33

K.[56] Is this effect limited to dislocation lines? Preparing films of slightly lower coverage with facets that have a small number of vacancies in their $\left(\sqrt{3}\times\sqrt{3}\right)R30^\circ$ coverage (Figure 2a,b), we observe rapid motion at similarly low temperature. The Supporting Information shows a movie. While increased diffusivity at high coverage has been observed in the past, to our knowledge it has not yet been quantified except at very low concentration[56] and for direct neighbors.[58,88,95] The confined nature of our exposed facets allows us to monitor the diffusion rate for a fixed numberdensity of molecules. The dotted line of Figure 3 shows the diffusivity from a few molecules per pore (Figure 2e,f) up to the point at which the $\left(\sqrt{3}\times\sqrt{3}\right)R30^\circ$ adlayer is one-third complete and site blocking becomes important (Figure 2c,d). While data points for coverages up to 6 molecules on the exposed facet were measured at 27 K, diffusion at higher coverages was too rapid at this temperature; the data point for 21 molecules per pore was measured at 22 K and scaled according to the Arrhenius parameters of ref 56. The dotted line represents an exponential fit of the diffusivity.

A detailed look at the STM images indicates that the diffusivity depends not only on the number of molecules on the exposed facet but also on the position of the molecules

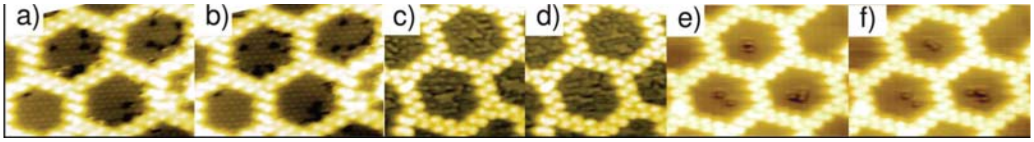

Figure 4.2: Images from STM movies showing the diffusion of (a,b) vacancies in a $\left(\sqrt{3}\times\sqrt{3}\right)R30^\circ$ CO coverage in confinement (image parameters, 12 nm × 9 nm; bias, -1.23 V; current, 120 pA, temperature, 23 K). (c,d) Twenty to twenty-two CO molecules on each exposed facet (image parameters, 8 nm × 8 nm; bias, -0.72 V; current, 60 pA, temperature, 22 K). (e,f) Two and three CO molecules in confinement (image parameters, 12 nm × 9 nm; bias, -2.67 V; current, 100 pA, temperature, 27 K).

within that facet. Generally, molecules tend to move less if they are closer to the center and more rapidly around the perimeter. Unfortunately, this renders a complete Arrheniusbased evaluation (which would need to separate molecules by location) beyond reasonable effort.

Thermally programmed desorption experiments showed that an increase of the surface coverage can lead to a reduction of the adsorption energy.[81] In the simplest approximation, the diffusion barrier is a constant fraction of the adsorption energy. While this argument justifies a variation of the diffusion barrier with coverage, it provides little indication that the diffusion preexponential factor should vary markedly with it. Fixing the diffusion prefactor at the value for isolated molecules,[56] the variation of the diffusion barrier with coverage can be obtained from the diffusion data (Figure 3, solid line). The adsorption and subdivision of the Cu(111) terrace by the anthraquinone network causes a reduction of the CO diffusion barrier by one-fourth; increasing the coverage inside the pore up to one-third of the $\left(\sqrt{3} \times \sqrt{3}\right) R30^\circ$ adlayer reduces the diffusion barrier by another one-fourth. The data suggests a linear fit of the reduction of the barrier as a function of the coverage with a slope of $(57 \pm 14)\,\%/ML$, with 1 ML defined as the complete $\left(\sqrt{3} \times \sqrt{3}\right) R30^\circ$ coverage. If the adsorption energy is assumed to be proportional to the diffusion barrier, then its reduction by half indicates a comparable reduction of the adsorption energy. The observation of a linear dependence of the energy reduction on the number density of molecules suggests that its origin is not direct pair interactions (which scale quadratically with coverage) but involves the substrate, potentially both through confinement-induced surface state effects[43,46,72] or through mediation of trio and higher order interactions.[68] While the effects of site blocking and nearest neighbor interactions prevent us from obtaining experimental data

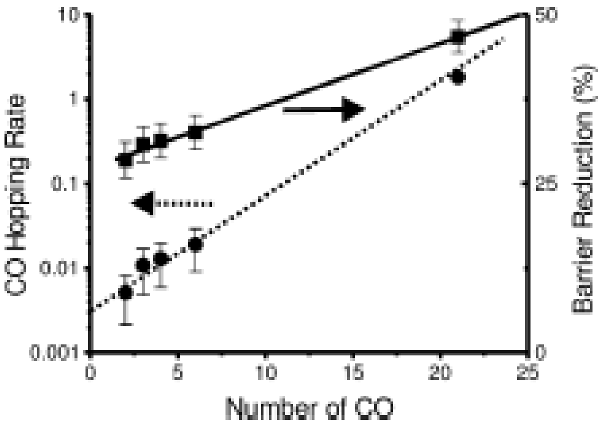

Figure 4.3: Dotted line: diffusion rate per molecule as a function of number of molecules on an exposed facet. Solid line: reduction of the diffusion barrier that causes this acceleration under the assumption of a constant diffusion prefactor. All error bars are dominated by the temperature uncertainty of 1 K in our measurements; the statistical error is much smaller than the data markers.

beyond 1/3 ML coverage, our results suggest a quite substantial destabilization of the CO molecules in the $\left(\sqrt{3} \times \sqrt{3}\right) R30^\circ$ adlayer, well in line with the results discussed in refs 81 and 95.

Following this discussion of the CO dynamics, we finally examine the locations that the molecules/vacancies occupy and the effect of the lateral confinement on them. To this end, we study the distribution of vacancies in coverages like the one shown in Figure 2a-d and of molecules in coverages like shown in Figure 2c,d; movies can be found in the online Supporting Information.

Figure 4a shows the likelihood that the dislocation line of Figure 1b-d occupies different substrate sites in a colorcoded histogram. In this context, it is important to realize that although the anthraquinone network appears 6-fold symmetric, due to the 3-fold (and not

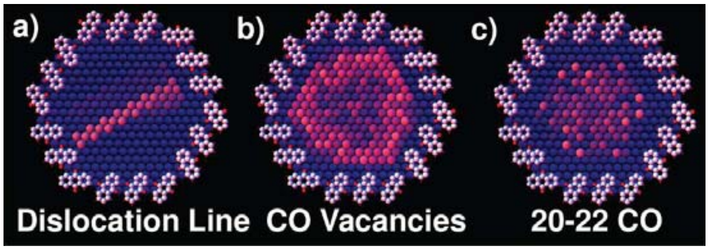

Figure 4.4: Color-coded histograms of CO vacancy/molecule distribution for each of the 186 Cu substrate atoms exposed within an anthraquinone pore. The anthraquinone pore is chiral and 3-fold symmetric, panels b and c are averaged over three equivalent rotational orientations. (a) Dislocation lines are most commonly found to cross the facet center, (b) whereas vacancies are more commonly found around the facet edge. (c) For 20-22 CO molecules, a relatively featureless distribution is observed. Each panel represents the location of >1000 vacancies/molecules.

6-fold) symmetry of the substrate, every other of its sides comes to rest at different surface locations. The dislocation line generally crosses near the center of the exposed facet thereby connecting dissimilar edges. Consequently, the area showing higher occupation of the dislocation line in the center right of Figure 4a is not equivalent to the area on the center left of the pore line. The sensitivity of the dislocation line to the geometry of the facet boundary is a testament to the importance of confinement for the spatial distribution of adsorbates. Figure 4b shows the distribution of vacancies on exposed facets a few molecules short of saturation; bright colors correspond to a high likelihood of finding vacancies. Viewing a large number of movies with coverages similar to Figures 2a,b, we qualitatively observe that the vacancies frequently arrange themselves in rows that originate at the facet edge and often bend back toward the same or an adjacent edge. In the histogram of Figure 4b, this is reflected in a higher probability for vacancies to be found at the edges with a slight preference for one kind of edge and vertex. It is important to realize that in our observation, the vacancies do not segregate from the adlayer, that is, they do not form a closely covered area surrounded by empty space as on extended terraces.[94] Rather the vacancies are interspersed with the adlayer, affecting a far greater fraction of the adlayer molecules and potentially rendering the adlayer more reactive. A statistical analysis of vacancy motion is much more complicated than for adsorbate motion, as in the $\left(\sqrt{3}\times\sqrt{3}\right)R30^\circ$ overlayer fractional vacancies (corresponding to molecules adsorbed in antiphase) can combine and molecules can occasionally and intermittently adsorb closer than the $\sqrt{3}$ spacing, so that the total number of vacancies on an exposed facet is not conserved.

Reducing the coverage to 20-22 molecules on the exposed facet (i.e., 1/3 of the $\left(\sqrt{3}\times\sqrt{3}\right)R30^\circ$ adlayer), we do not observe aggregation into large islands (Figure 2c,d). Despite the low temperature, only small aggregates of molecules form, with almost every molecule being accessible on the surface from at least one side (see Supporting Information). This is, again, in marked contrast to CO films on extended terraces, where we find extended $\left(\sqrt{3}\times\sqrt{3}\right)R30^\circ$ islands under similar conditions.[94] The distribution of molecules within the exposed facet is relatively featureless; no preferred or avoided regions of adsites can be discerned (Figure 4c).

4.4 Conclusion

In summary, we conducted a survey of the effects that nanometer-scale confinement can have on adsorbate dynamics and placement; on small exposed facets we found that adsorbate diffusion increases rather than decreases, resulting in more even and open distributions of adsorbates and adlayer vacancies than found on extended terraces. Even at full coverage, confinement can stabilize dislocation lines that affect a substantial fraction of the molecules in the adlayer (more than one-fourth of them). In combination, these findings suggest that confinement alone can increase the potential for surface reactivity in an adsorbate film: the smaller the facet size (i.e., the smaller a metal nanoparticle that creates it), the more pronounced the mentioned effect.

Chapter 5

Acetylene on Cu(111): Imaging a Molecular Surface Arrangement with a Constantly Rearranging Tip

This chapter is taken from one article I published on *JOURNAL OF PHYSICS: CONDENSED MATTER, 24, 354005 (2012).* This is the first time I dominantly take care of one research project. As the first author of this paper, in this project, I did the most of sample preparation and experimental measurement with the assist from graduate students (Quan Ma, Dezheng Sun) and undergraduate student (KatieMarie Magnone), meanwhile, the theoretical simulation is come from graduate students (Jonathan Wyrick, Kamelia D Cohen) and undergraduate students (Connor Holzke, Daniel Salib).

5.1 Introduction

Acetylene is one of the platform chemicals of todays chemical industries; innumerable everyday compounds as well as specialty use ones can be traced to acetylene as a foundation feedstock.[97] A significant portion of the processes by which these are made relies on heterogeneous catalysis, and copper is a metal found in many industrial catalyst compositions. This renders understanding the interaction of acetylene with the thermodynamic equilibrium (111) surface of copper an obvious goal. Furthermore, acetylene is one of only a few (organic) molecules with 4 atoms or less and thus presents an excellent model system to study fundamental metal-organics interactions at limited complexity. In this manuscript, we describe real-space scanning tunnelling microscopy (STM) investigations of acetylene on Cu(111) and apply density functional theory (DFT) modelling to elucidate the particular STM imaging mode in the presence of an acetylene molecule at the tip apex. Prior investigation revealed that acetylene adsorbs on Cu(111) with its carbon-carbon bond lying across a bridge site [98, 99] and with its hydrogen atoms each pointing away from the surface as shown in figure 1a, in contrast to the linear character of acetylene in the gas phase. Isolated acetylene molecules have been imaged on Cu(111) by Konishi et al. [100] and on Cu(100) by Stipe et al. [101]. At higher coverage, reciprocal space data, i.e., low energy electron diffraction (LEED) [1], indicates a $\begin{pmatrix} 2 & 1 \\ 0 & 4 \end{pmatrix}$ pattern (figure 2a) [1]. It was proposed that this pattern corresponds to two molecules per unit mesh, thus a coverage of 0.25 ML, which is consistent with the previously-known local geometry involving bonding of each molecule to four Cu atoms. Following the theme of this special issue from reciprocal to direct space, this manuscript provides real-space validation of this arrangement and explores fundamental aspects of the acetylene substrate interaction.

Imaging acetylene coverages on Cu(111) we find a pronounced sensitivity of the STM image to the tip condition in a very particular way: acetylene is found to form rows of molecules, as predicted by LEED, but the contrast between adjacent rows varies considerably, sometimes making them appear practically identical, sometimes fundamentally different. This prevents direct correlation between an STM image and any particular adsorption structure; no information on the molecular orientation or registry in neighbouring adsorption rows can be obtained in a straight-forward way from STM images. Using DFT modelling of the adsorption configuration, we are able to show that the particular imaging contrast is caused by attachment of an acetylene molecule to the STM tip apex in a fashion that allows it to adjust itself dynamically to the orientation of the substrate acetylene rows directly underneath the tip, thus generating an image transfer function sensitive to the local rotational orientation of the surface setup.

Variation of imaging conditions induced by the transfer of non-metallic species on the tip apex was first reported two decades ago by Eiglers group in the context of experiments in which Xenon atoms acted as atomic switches.[102, 103] Molecular adsorption has been shown by Rieders group to provide chemically sensitive contrast[70] and, since then, numerous contrast modes in STM based on related phenomena have been reported.[104-106] We believe that these findings for acetylene are distinct to the extent that they involve dynamic reorientation of the molecule at the tip apex in a fashion determined by and sensitive to the rotational orientation of the adsorbates. Modelling this behaviour, we can achieve

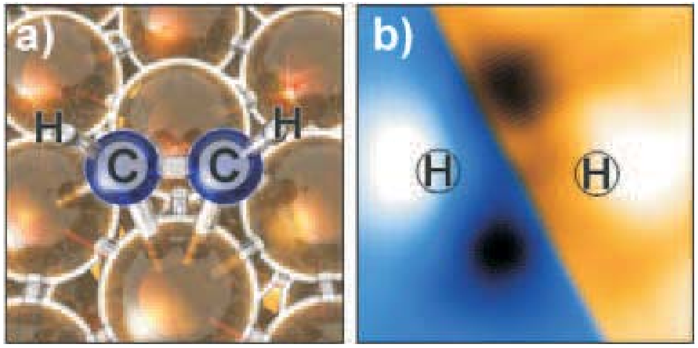

Figure 5.1: (a) DFT-simulation of acetylene adsorbed on a Cu(111) bridge site. (b) simulated image (bottom left, blue) and STM image (top right, orange) of an isolated acetylene molecule on Cu(111) highlighting the good correspondence between simulations and measurement; STM Parameters: Bias = -1.9 V, Current = 0.1 nA, Image Size = 8 Å× 8 Å.

high-fidelity agreement with the images obtained by STM, confirming the predictions from LEED measurements in real space and ruling out the presence of alternative adsorbate periodicities.

5.2 Experimental Setup

All STM measurements proceeded on a Cu(111) substrate cleaned by cycles of sputtering and annealing. The cleanliness of the sample was ascertained by imaging at ∼85K followed by exposure to 10^{-8} Torr for 1.5 minutes (∼ 0.9 Langmuir) of acetylene (99.6% pure, Airgas) on the cryogenic sample. Immediately following exposure, the sample was allowed to warm to room temperature over 45 minutes for annealing of the adsorbate coverage, and then re-cooled for imaging. Electrochemically edged tungsten wire was used as tip material.

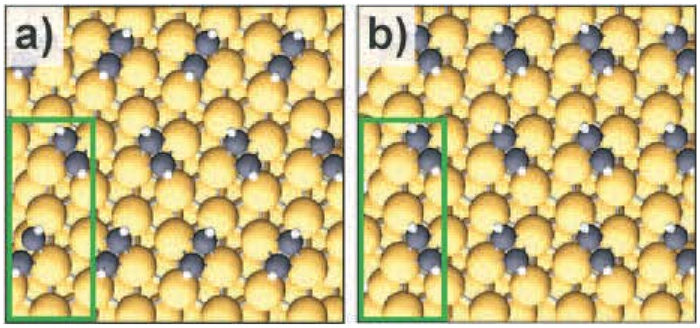

Figure 5.2: (a) adsorption geometry of acetylene on Cu(111) as predicted from LEED measurements [1]; (b) alternative adsorption geometry potentially compatible with STM images. The green boxes in (a) and (b) indicate the lateral dimensions of the supercells used in calculations.

DFT calculations use the VASP code[107-110] with the Generalized Gradient Approximation (PBE-GGA) approximation[111, 112] for the exchange-correlation functional and a projector-augmented-wave (PAW) basis[113, 114]. All results are optimized so that the remaining forces are less than 0.03 eV/Å. Simulations of STM images use a 6 layer slab separated by 23 Åof vacuum in the same supercell as figure 2a on a $13 \times 7 \times 1$ k-point mesh with plane wave and augmentation charge energy cutoffs of 600 and 2000 eV respectively. Calculations to assess acetylene-substrate interactions use different supercells and k-point meshes as indicated below.

5.3 Results and Analysis

Figure 3 shows a selection of STM images acquired on a sample with 1/4 monolayer (ML) acetylene (with 1 ML taken as one adsorbate per substrate atom). Depending on the tip condition, the parallel rows of protrusions appear to have either identical or heights. These images pose two questions: a) can the rows observed by STM be identified as adsorbates aligned in parallel in each row but featuring alternating orientation in neighbouring rows as predicted by the LEED data (figure 2a) [96], thus ruling out an alternative $\begin{pmatrix} 2 & 1 \\ 0 & 2 \end{pmatrix}$ pattern of identically aligned molecules (figure 2b), and b) why are in some cases the molecular rows imaged identically while in others a pronounced difference is observed.

5.3.1 Identification of adsorbate pattern by STM image simulation

We first address whether the adsorbate arrangement of figure 2a is actually capable of producing the variety of images we observe in STM, of which a subset is shown in figure 3. Clearly a sharp metallic tip cannot provide the variation in contrast between neighbouring rows that is observed. Thus, we explore the imaging properties of an STM tip decorated with an acetylene molecule at its apex, a likely occurrence when scanning an acetylene-covered substrate. Here it is important to consider the image of an isolated acetylene molecule (figure 1b), which consists of two areas of high tunnelling probability separated by ~2.5 Åwhile the remainder of the molecule has lower (or similar) tunnelling probability than the underlying substrate. In the s-wave approximation of the Tersoff and Hamann interpretation of the STM current signal [115], the STM tip contours a surface of constant charge density integrated between the tips and the surfaces Fermi level (whose difference is given by the applied bias). This approximation has been shown to be successful in many cases, yet to be lacking for cases with more complex interaction between substrate and adsorbate electronic states.[105, 116-119]

Tersoff and Hamann showed that under the assumption of an s-type wave function at the tip

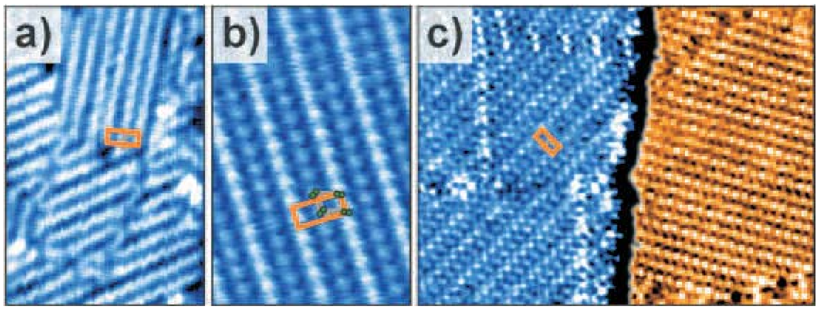

Figure 5.3: 1/4 ML coverage of acetylene on Cu (111). STM Parameters (a): Bias = -1.07 V, Current = 96 pA, Image Size = 6.2 nm x 9.3 nm. (b) Bias = -0.66 V, Current = 0.11 nA, Image Size = 4.2 nm × 6.3 nm. (c) Bias = -1.07 V, Current = 0.11 nA, Image Size = 16.7 nm × 12.5 nm. Differences in the appearance of (a), (b) and (c) are due to tip conditions to be discussed. Adsorption positions of the acetylenes are shown in (b) with circles representing the carbon atoms connected by a parallelogram (grey). The unit mesh is indicated with a rectangle (orange).

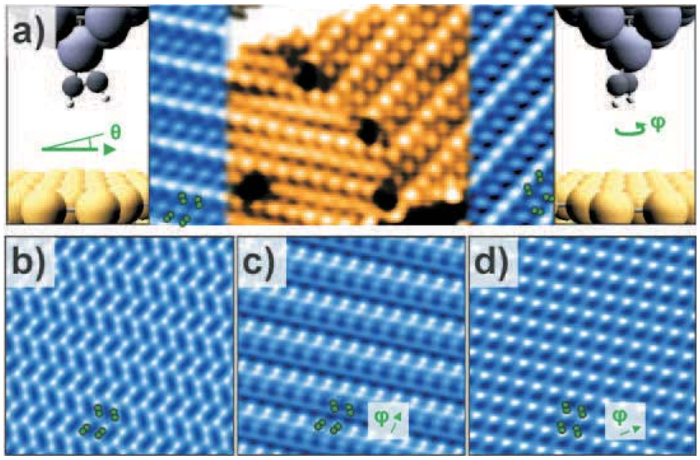

Figure 5.4: (a) The centre panel (orange) shows an STM image of a boundary between two rotational domains of an acetylene coverage on Cu(111), which is at the left and right edge continued (blue) with simulated STM images using the tip geometries shown on the respective sides; Tip Parameters: $\theta = -4°$ (left) $+4°$ (right); STM Parameters: Bias = -1.1 V, Current = 0.10 nA. (b) The pattern on the left of (a) modelled with a point-like tip. (c) The same pattern, but with an adsorbed acetylene at the same angle $\varphi \sim 25°$ (as measured from the panel vertical) used on the right of panel (a). (d) The pattern of figure 2b under the same conditions used to generate the left of panel (a): $\varphi \sim 70°$.

apex, the surface of constant energy-integrated charge density can be determined by treating the tip as an infinitely sharp point. This approach can be amended straightforwardly to the case that an acetylene molecule is attached at an in-plane angle φ and an out-of-plane angle θ to the tip: rather than sampling only at one point, we sample the calculated charge density with a pair of Gaussians spaced apart like the apparent height maxima of an acetylene molecule on Cu (111) oriented in space according to the angles φ and θ. Figure 4a shows an example: the (orange) centre part of the image was acquired by STM and the (blue) sides of the panel are simulated STM images using the acetylene configurations on the tip apex shown in the left and right of the panel. In both cases the acetylene molecule is titled by $|\theta| = 4^\circ$ relative to the substrate but its rotational orientation on the tip apex differs by 60°. Recognizing the different adsorption geometry of the acetylene molecule is tantamount to obtaining meaningful correspondence between experiment and modelling: using a standard s-state (point-like) tip, the image of figure 4b is obtained; modelling the left part of figure 4a with the same orientation of the tip acetylene molecule as on the right, the image of figure 4c is obtained; using the adsorption arrangement of figure 2b with the same tip conditions as the left of panel yields the image of figure 4d. Neither figure 4b nor 4c is a faithful representation of the rotational domain on the left of panel a, and the image of figure 4d associated with the alternative adsorption periodicity (figure 2b) is not seen experimentally. As the STM image in panel a was scanned in horizontal lines, this finding implies that not only was an acetylene molecule present at the tip apex, but also that it reoriented itself in response to the alignment of the adsorbate rows on the substrate in every scan line at high fidelity.

This approach to simulating STM images is not limited to the particular STM image observed in figure 4a. We repeated this procedure for a wider range of STM imaging conditions than the sampling in figure 3 and were in each case able to obtain convincing correlation. Figure 5 shows two additional examples. Figure 5a corresponds to figure 3a and can clearly be modelled at high fidelity using a horizontal acetylene molecule ($\theta = 0°$) at the tip apex. In contrast, the rather disordered arrangement in the centre of figure 5b is faithfully extended using a tilted acetylene molecule ($\theta = 45°$) on the tip. The geometric parameters used in each case were those which most faithfully reproduce the acquired STM images.

5.3.2 Identification of substrate strain as determining adsorption ordering

Having validated that the images of acetylene/Cu(111) are indeed consistent with the predicted $\begin{pmatrix} 2 & 1 \\ 0 & 4 \end{pmatrix}$ acetylene surface pattern, we turn to the origin of the different orientations of the acetylene species in each unit mesh. To this end, we compare DFT simulations of both adsorption configurations of figure 2 in supercells of identical size and geometry. Comparison between systems, in which the molecules are attached and lifted from the substrate yields a binding energy per acetylene molecule of 2.35 eV for the structure predicted by LEED (compared to 2.29 eV for the configuration of figure 2b), providing an energetic explanation for this preference.

In both super meshes the molecules are sufficiently separated from one another ($\sim$ 5Å) that their interaction has to be dominated by substrate-mediated components. Prior work

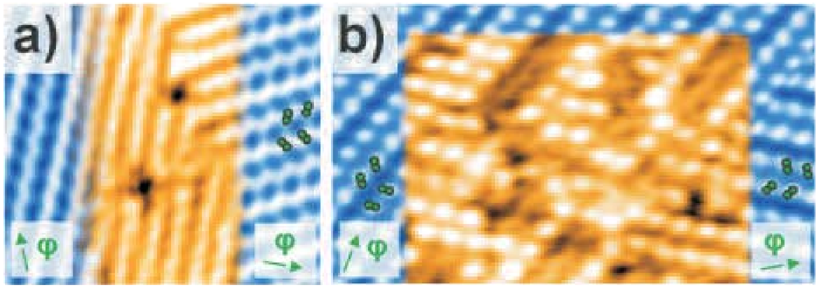

Figure 5.5: Comparisons between STM images (centre, orange) and model (sides, blue). (a) Model Parameters: = 0; STM Parameters: Bias = -0.66 V, Current = 0.11 nA. (b) Tip Parameters: $\theta = 45°$; STM Parameters: Bias = -0.99 V, Current = 0.10 nA.

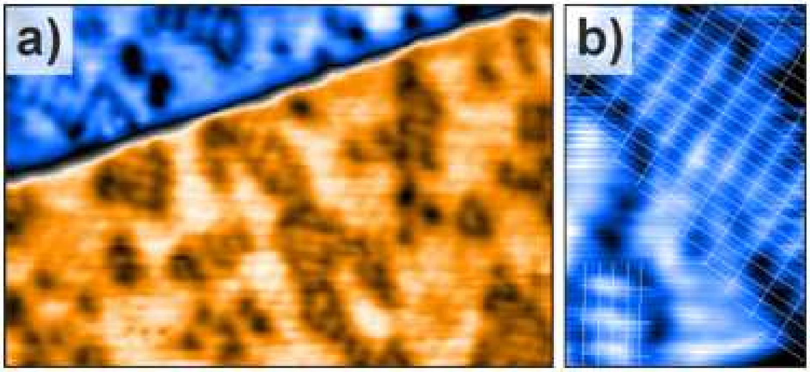

Figure 5.6: Acetylene at ∼1/8 ML coverage on Cu (111). (a) Island formation is observed. (b). The islands are composed of rows of molecules of the same periodicity found at elevated coverage, indicated here with white grid lines. STM Parameters (a): Bias = -0.83 V, Current = 0.10 nA, Image Size = 16 nm × 11 nm. (b): Bias = -1.0 V, Current = 0.12 nA, Image Size = 3.9 nm × 5.8 nm.

showed that acetylene adsorption induces stress in a Cu(111) surface that is directed perpendicular to the molecular axis, attempting to widen the span of the bridge (site) the molecule inserts itself into [120]. Using 3 atoms thick copper slabs in our calculations, we find that indeed the system is under in-plane compressive strain. Allowing the supercells to artificially expand to equilibrium in 2D (which in reality would be forbidden through interaction with the underlying bulk), the energetic difference between the orderings of figures 2a,b vanishes to < 1 meV, i.e., beyond the expected resolution of our calculations. In this process, both unit meshes expand by nearly the same amount (1% and 2% along the short direction and long direction as indicated in figure 2, respectively). Thus, the energetic difference between the two adsorption orderings can be attributed to differences in the resultant compressive stress on the lattice; it is energetically unfavourable when all molecules are aligned in parallel and their stress vectors add up.

5.3.3 Aggregation of acetylene molecules due to long-range substrate mediated interaction

Assignment of the adoption of the observed adsorbate arrangement and periodicity to release of surface stress poses the question whether the ordering is solely governed by repulsive interactions. While ordering based on repulsive intermolecular interactions is conceptually possible in the presence of a dominant interaction anchoring the molecules to the substrate, it generates a more tenuous foundation for large scale order, as any set of vacancies is not expelled to the outside of the adsorption structure. To investigate whether net attractive interactions between adjacent acetylene molecules also exist on Cu(111) we prepared incomplete coverages (figure 6, ∼1/8 ML acetylene). Here acetylene molecules aggregate into small islands and, more frequently, into the same pattern of adjacent rows, that feature the same periodicity found at 1/4 ML coverage (figure 6b). The formation of such aggregates indicates the presence of attractive interactions. Thus, in addition to the surface stress that orients the molecules in dissimilar orientations, there are also attractive interactions between the molecules present. Given the comparatively large intermolecular distance in this structure, these interactions need to be mediated by the substrate.

Rieders group and others have shown [53-61,63,67,77,122-126] that the substrate is capable of mediating attractive forces over distances far greater than the size of individual atoms or molecules. Following Ref. [60], we test whether the variation in total system energy E' between different configurations of acetylene molecules on Cu(111) can be described by the sum of substrate-mediated pair interactions:$E' = \sum_r E_{pair}(r)$,where r ranges over the set of all pair-wise distances between acetylene molecules on the surface. For such systems a pair interaction energy function (1) has been proposed [127], where A represents the overall interaction amplitude, k its periodicity, δ its scattering phase and r the pair distance. This approach is unable to describe short-range interactions correctly, as they are important for the order formation. To account for this we define a set of 5 shortest distances $r_i = \{1, \sqrt{3}, 2, \sqrt{7}, 3\} \times 2.55$ Åfor which Epair is defined explicitly:

$$E_{pair}(r; \varepsilon, A, k, \delta) = \begin{cases} \varepsilon_i & \text{if } r = r_i \\ \frac{A \sin(2kr+2\delta)}{r^2} & \text{if } r > r_5 \end{cases} \tag{5.1}$$

In order to test whether such an interaction may cause the ordering of acetylene into the rows observed we calculated the total energy of 24 different relative locations of two acety-

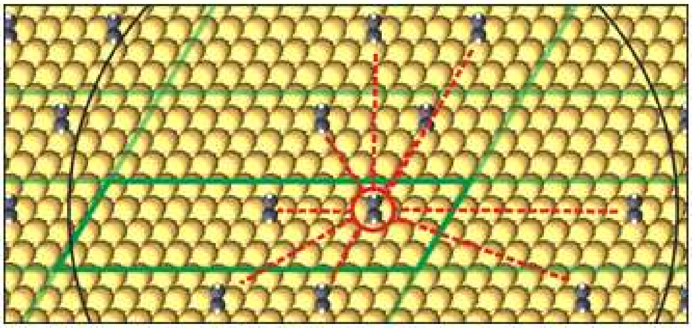

Figure 5.7: Setup for calculation of the surface state mediated interaction. Dashed red lines indicate the pair interactions. A black circular outline indicates the cutoff radius of 30 Åused. For simplicity, only the interactions for the circled acetylene are shown, and only those interactions between acetylenes visible in the frame.

lene molecules on 14 × 4 × 3 copper atoms slabs (figure 7 shows an example). To limit configurational and computational complexity, we only considered molecules in the same orientation on the surface and one k-point, respectively. Depending on the intermolecular spacing, we find a variation of the total energies by ∼0.1 eV with the exception of the case for directly adjacent acetylenes (separated by one substrate atomic spacing only), for which the total energy is higher (less favourable) by ∼0.6 eV. The supporting information shows the supercells evaluated and the total energies found.

We find the interaction potential E_{pair} by fitting its 3 variables and 5 explicitly defined values to achieve a best match of E for all 24 super mesh geometries considered simultaneously. Here we include interactions between acetylene molecules and their copies in neighbouring unit meshes up to a distance of 30Å(figure 7). The optimal values for the parameters are A = 2.1 eV, k = 0.33 $\mathring{A}^{-1}$, $\delta = 0.7\pi$. The resulting interaction potential is shown in figure 8; the vertical lines indicate the intermolecular separations present in our set of relative acetylene locations. By evaluating the rms error in the fit of the set of 24 configurations, we can estimate the error band of our fit (see supporting information). Figure 8 reveals a pronounced (∼0.05 eV) attraction at separations of ∼ 5 Å, the intermolecular spacings in the experimentally observed surface structure, followed and preceded by repulsive interactions. Given that only molecules of one orientation were considered, the particular separations found at molecules in neighbouring rows of 5.6 Åwas not tested explicitly but falls into the attractive region of E_{pair}.

The optimal fit value of the periodicity k of 0.33 $\mathring{A}^{-1}$ is in reasonable agreement with the sp-band and surface state Fermi wave vector on the Cu (111) surface of 0.26 $\mathring{A}^{-1}$ and 0.22 $\mathring{A}^{-1}$ [77], respectively. In Rieders and others work [53-61,63,67,77,122-126] long range interactions on Cu(111) were ascribed to the surface state and it is also a likely candidate here. However, including only 3 substrate layers in our simulations (although resulting in >160 substrate atoms per supercell investigated) does not allow us to distinguish between the sp-band and surface state: as shown by Berland et al., [128] the surface states on the top and bottom of a slab can only clearly be distinguished from the bulk states and one another with a minimum of 6 copper layers (and only then with appropriate transformations of the Kohn-Sham states). Consequently, our simulations do not permit direct attribution of this effect to the Cu(111) surface state. Experimentally, the propensity for acetylene to form odd-shaped aggregates prevents a meaningful analysis of STM images by pair correlation function to obtain experimental verification of the parameters of Epair. Nevertheless, the data of figure 8 is a clear indication that acetylene adsorbates generate a net attractive interaction between species at a certain distance, despite causing a compressive strain on the

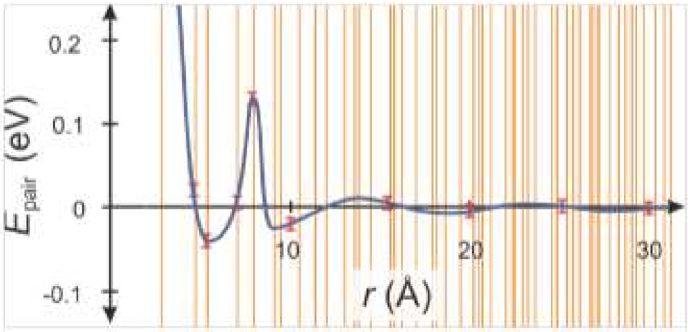

Figure 5.8: Interaction potential Epair. Vertical lines indicate distances sampled. The error bars correspond to ∼ ±0.01 eV fit error.

top substrate layer. As such they provide a theoretical underpinning for the experimentally observed molecular arrangement.

5.4 Conclusion

We have shown that validation of a diffraction-derived surface pattern [96] of acetylene on Cu(111) by STM is possible, if the modification of the STM image transfer function through the adsorption of an acetylene molecule onto the tip apex is taken into account. In that case, the images of acetylene coverages on Cu(111) also include direct evidence of the rotational orientation and dynamics of the acetylene species attached to the tip apex. DFT modelling of acetylene/Cu(111) reveals that the molecular orientation and separation is governed by a balance of repulsive interactions associated with stress induced in the top surface layer and attractive interactions mediated by the electronic structure of the substrate. Computationally relatively inexpensive modelling of the substrate with 3 layers allows one to obtain the periodicity of the intermolecular interaction that is in reasonable agreement with experimental values of the band structure of copper.

Chapter 6

Metal-Organic Coordination on 2-D Cu(111) Surface: 2-cyanonaphthalene (CN) *vs.* 2-isocyanonaphthalene (ICN)

6.1 Introduction

A metal-organic coordination pattern & network on a metal surface is studied in recent decades because of its very important role as the bridge from traditional adsorbate patterns in the Angstrom scale to nanometer patterns or even larger, which is an area of cutting-edge research in catalysis.

Many resultant coordination patterns & networks based on molecules with different organic

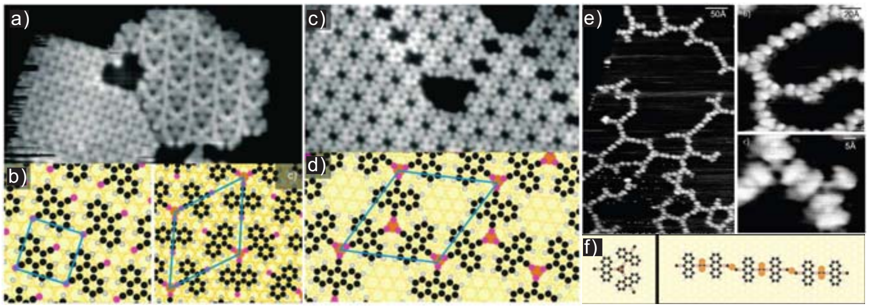

Figure 6.1: a) STM image of DCA on Cu(111) obtained at 180 K (175×95 Å, -2.6 V, 0.22 nA), depicting separate regions of the α phase (left) and β phase (right). b) DFT minimization of the adsorbate patterns (α and β phase) with the unit cell indicated. c) STM image (180×100 Å, -3.8 V, 57 pA, 30 K) of the γ phase of DCA on Cu(111). d) Corresponding model of γ phase. e) STM image of random mesh structure at high DICA coverage on Cu(111) obtained at 85 K (1.3 V, 81 pA). f) Proposed model for triangle motif and chain motif

ligands and metal adatoms are reported, illustrating the large extent of this interesting research area and the chemical, physical principles behind it. However, in this chapter, a new research perspective will be introduced. By comparing the coordination patterns having the same metal adatoms and highly similar organic ligands (cyano- and isocyano species), the contribution from the organic ligands to the coordination patterns is more directly revealed.

As shown in Fig 1, in the previous studies, the coworkers P. Greg and M. Luo in our lab have alrealdy found that Cu-DCA (Dicyanoanthracene) and Cu-DICA (Diisocyanoanthracene) coordinations form significantly different network structures on Cu(111) surface. While the high coverage Cu-DCA coordination forms three different ordered and periodic arrays of molecules featuring three unit cell phases, the Cu-DICA can only generate a sparse random mesh structure with triangles and short chains, which directly indicate the contribution from the different ligands to the coordination bond properties. However, most of the chemical features and properties that lead to this difference are still in unaccounted for. In order to further simplify the system, in the study of this chapter, a new pair of organic molecules is chosen, 2-cyanonaphthalene (CN) and 2-isocyanonaphthalene (ICN).

6.2 Experiment Setup

For the data shown in this chapter, All the STM images are taken at liquid nitrogen (LN_2) temperature (∼85K). The Cu(111) substrate is cleaned by sputter / anneal cycles, and then directly cooled down to LN_2 temperature to check for flatness and clenliness. After dosing the organic molecules which are sublimed from a line-of-sight glass tube, the sample is subsequently annealed to room temperature (∼298K) in a UHV chamber, so that the Cu adatoms at the edge of terrace can have enough energy and be free to form the coordination compounds on the sample surface.

For the theoretical simulations, we used the VASP code[107-110] with the PBE-GGA[111, 112] exchangecorrelation functional and a projector-augmented-wave (PAW) basis[113, 114]. Calculations were performed for each compound coordinated to a Cu adatom at an fcc hollow on a 2-layer Cu slab, 8x8 atoms in the lateral dimensions. All results are optimized so that the remaining forces are less than 0.03 eV/$\mathring{A}$. Large super-cell dimensions allowed us to sample k-space exclusively at the gamma point (due to a respectively small Brillouin zone). Plane wave and augmentation charge energy cutoffs of 400 and 700 eV, respectively, were used.

6.3 Result and analysis

Even though the project is still not finished yet (more STM images and theoretical calculations are still processing), the existing results are already able to reflect the difference between these two ligands and some of the chemical properties behind those differences.

6.3.1 Comparison at low coverage

As shown in fig 2, after annealing the sample to room temperature, coordination compounds of 3-, 4-, 5-, and 6- fold patterns for both species appear on the surface. For both species, 5-, and 6- fold compounds may require more than one adatom, due to the limitation of the 2-D space. Theoretical simulations are still needed to investigate the detailed properties, however, the irregular shape of these 5-fold compounds shown in fig 3 somehow gives a deficient evidence of this assumption. For the smaller compounds, such as 3- fold and 4-fold, different configurations of coordination compounds with the same number of ligands are found on the substrate, which indicate that the space limitation of the asymmetric molecules lying on the 2-D Cu(111) substrate gives these a property of chirality. Theoretical calculations of the preference and energy difference of these two different chiralities are still needed.However, expect these similarities, the major difference

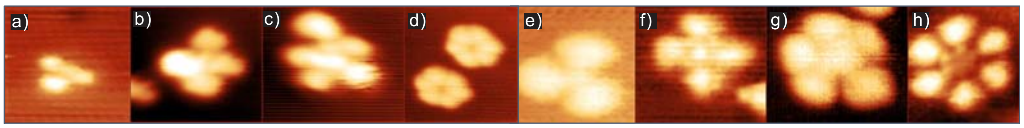

Figure 6.2: The left four images a)-d) are 3-6 fold coordination patterns for isocyano compounds, the right four images e)-f) are the same patterns but for cyano compounds

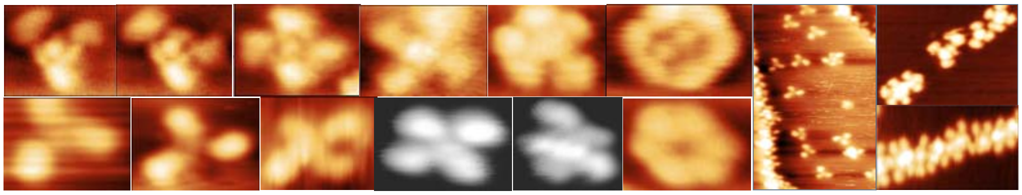

Figure 6.3:

between these two coordination compounds is shown in Fig.3. For isocyano compound, all the coordination patterns are individual, none of them are found next to each other, while for cyano compound, these chain structures indicate that the coordinate patterns can stay so close to each other that make us hard to identify the real Cu adatoms.

Density Functional Theory (DFT) calculations are used to extract the binding energy per ligand, the total binding energy and variation in the ionic relaxation of the coordination center with coordination number. As shown in Fig. 4(a)(b), as predicted, the total binding energy increases as the increasing of bond number, and the binding energy per ligand decreases since the 2-D surface limits the ligands to occupy the optimal position, which reduce the binding energy. The different nature of Cu adatom coordination of the cyano and isocyano species manifests itself in varying degrees of lifting of the inward relaxation of the Cu adatom. The significant difference shown in Fig.4(C) between 3-fold and 4-fold of isocyano compounds matches the preference of 3-fold at low coverage as shown in Fig.3, meanwhile, there is no this preference shown in cyano species.

Detail DFT calculation shows the evolution of the charge redistribution at the coordination of a single Cu adatom by 1-4 fold isocyano- (left) and cyano-naphthalene (right) molecules,

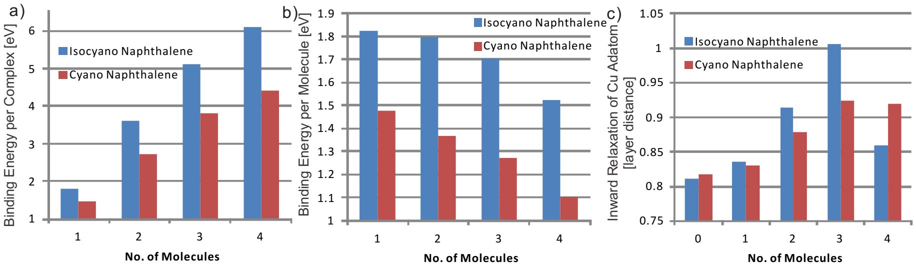

Figure 6.4: DFT calculations results a). extract the binding energy per ligand (decrease with increasing coordination number), b). the total binding energy (increasing with increasing coordination number) and c). variation in the ionic relaxation of the coordination center with coordination number

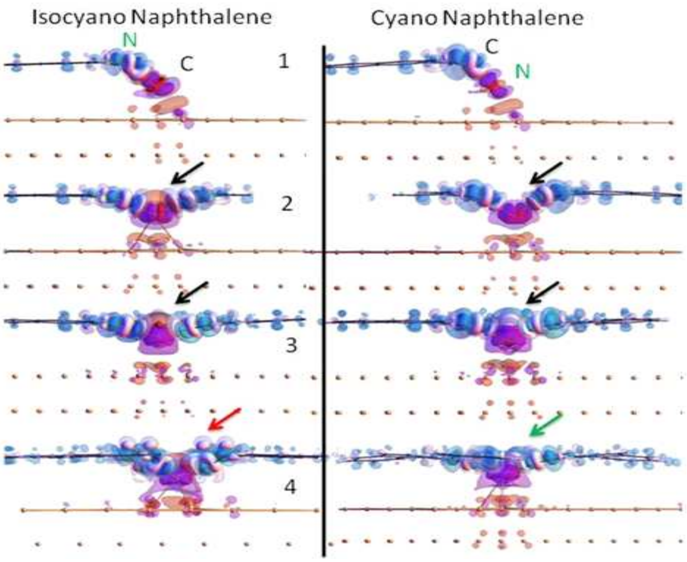

Figure 6.5: DFT calculation results of the charge redistribution at the coordination of a single Cu adatom by 1-4 fold isocyano- (left) and cyano-naphthalene (right).

which help us to understand why the 4-fold isocyano compound is disfavored. As shown in Fig.5, for isocyano compounds charge accumulates atop the Cu center (black arrow) since the electronegativity of isocyano group, which is not the case for cyano species. These charge accumulation leads the 4-fold coordination to an unphysical charge redistribution in the ligands for isocyano groups (red arrow).

6.3.2 Comparison at high coverage

Similar as the comparison of DCA and DICA, at high coverage, the STM images intuitively exhibit the difference between cyano and isocyano species. As shown in Fig.6(a), for the isocyano compounds, the dominate coordination pattern, 5-fold structures randomly and individually locate on the surface. Same as in the low average, none of the coordination patterns are close to each other, even under such high coverage. The solution for isocyano compounds to respond the space limitation is accepting more ligands for one coordination pattern, even though there are disfavored under low coverage.

However, in Fig.6(b) high coverage cyano coordination patterns exhibit the properties of both DCA and low coverage, ordered and close with each other. The long range ordered periodic network also matches the 3-fold symmetry property of Cu(111) substrate, which indicates more interaction between coordination network and substrate. Under the space limitation, different from the isocyano compounds, cyano coordination compounds forms closer network to reduce the space cost. From the zoom in image Fig.6(c), the two different orientations of 3-fold network may also relate to property of chirality. The clear exist of 4-fold coordination pattern matches the DFT calculation prediction, that even though 4-

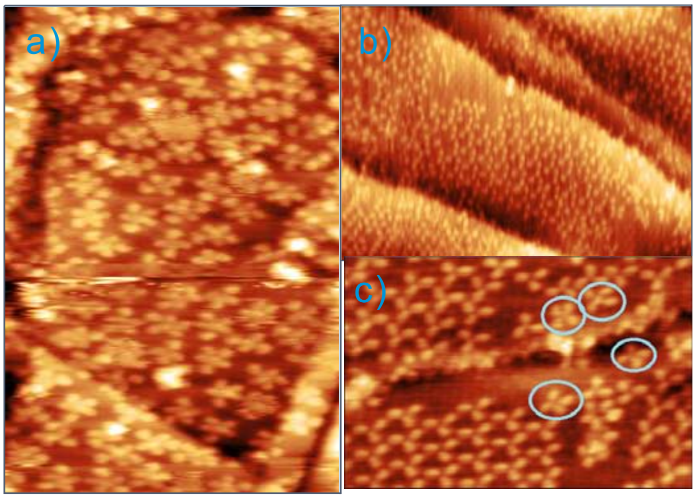

Figure 6.6: a) STM image of high coverage isocyano patterns on Cu(111) obtained at 40 K (-1.6 V, 49 pA). b) STM image of high coverage cyano network on Cu(111) obtained at 85 K (-1.0 V, 99 pA). c) high resolution images of cyano network.

fold is not the most favorite option, similar inward relaxation of the Cu adatom with 3-fold allows its appearance.

In order to investigate the lack of long-rang periodic network at high coverage and close pattern at low coverage for isocyano species, a detail DFT calculation of charge transfer along the naphthalene molecule is made. As shown in Fig.7, the 5-, 6- C-H bonds (red arrow) are almost electroneutral in the cyano species. Meanwhile, for the isocyano species, both of these two bonds have charge density. Since these two bonds are most far away from the coordination center, which are most likely interact with other coordination patterns, we believe the electroneutral property allow the cyano coordination pattern to stay close to each other, even generate network.

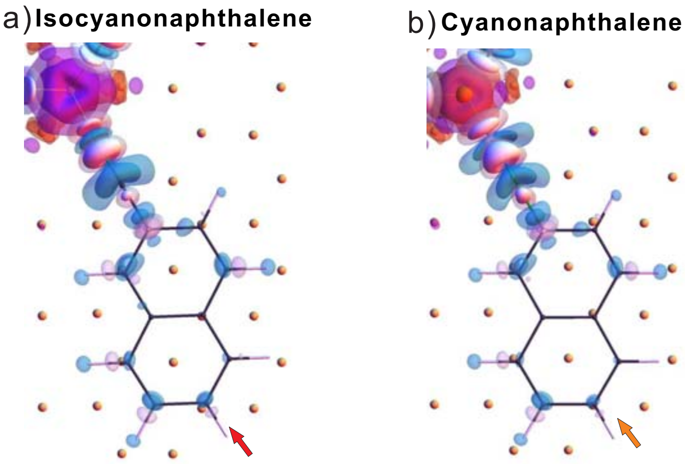

Figure 6.7: calculation of charge transfer along the naphthalene molecule for isocyano- (left) and cyano-naphthalene (right)

6.4 Conclusion

In summary, with the same backbone naphthalene but different coordination ligands, cyano / isocyano, Cu adatoms exhibit different coordination patterns under STM. DFT calculation about the binding energy, local charge transfer, and inward relaxation of the Cu adatom affords more chemical properties behind these differences. More theoretical modeling may provide a more detail explanation on configuration and chirality. Also more low coverage STM images of cyano compounds are still need for more comprehensive comparison.

Chapter 7

Controlled argon beam-induced desulfurization of monolayer molybdenum disulfide

STM is not the only instrument for surface science. This chapter is taken from one article I published on *JOURNAL OF PHYSICS: CONDENSED MATTER, 25 252201 (2013)*, which is the research project I cooperate with Ph.D students Quan Ma, Patrick M Odenthal, and John Mann, using PL, Raman and XPS spectrums to characterize the property of monolayer MoS_2 grown by CVD. My contribution in this project is characterizing the band gap shift with the three spectrums.

7.1 Introduction

Molybdenum disulfide, MoS_2, has attracted widespread attention as one of the interesting atomically thin materials beyond graphene [129131]. Like graphene, it can be prepared in a stable form down to monolayer thickness. In contrast to graphene, however, MoS_2 has an intrinsic band gap: the indirect bandgap of bulk MoS2 of ~ 1.4 eV crosses over to a direct optical bandgap of ~ 1.9 eV in the monolayer limit [132, 133]. In addition to this interesting electronic structure, MoS_2 has many established applications in catalysis, such as for hydrodesulfurization [134, 135], and it recently received attention as an electrode material for water splitting [136, 137].

Single-layer MoS_2 field effect transistors have been fabricated with mobilities on the order of $1cm^2V^{-1}s^{-1}$ and higher [138141], as well as onoff ratios up to 10^8 at room temperature. Bulk MoS_2, and most mono- or few-layer MoS_2 materials examined to date, exhibit n-doping [138143], but p-doping has also been observed [144]. Ambipolar operation has been achieved by gating with an ionic liquid [145]. Another distinctive electronic property is the possibility of selective valley population of the monolayer, which has been achieved using excitation by circularly polarized light [146150].

Although many of the studies to date have made use of mechanically exfoliated single-layer MoS_2 films [151], MoS_2 monolayers can also be prepared by means of chemical vapor deposition (CVD). A variety of substrates, including Cu [152], Au [144, 153155], SiO_2 [144, 156], and various other insula tors [141, 144, 157], have been successfully used for growth. Molybdenumsulfur compounds with stoichiometry different from MoS_2 have been reported in CVD deposition, including Mo_6S_6 nanowires [158, 159] and Mo_2S_3 films [160, 161].

Like graphene, single-layer MoS_2 is stable in air for extended periods of time. In carbon-based materials, such as nanotubes and graphene, this high stability, while attractive for many purposes, has proven a challenge for other needs. Intense processing is required, for example, to bond covalently to these materials, to render them soluble, and to alter their electronic properties, such as by hydrogenation or partial oxidation of graphene. For MoS_2, the inertness of the basal plane calls for interventions to facilitate chemical reactions. In this regard, theoretical studies indicate that sulfur vacancies are reactive [162, 163]. In this paper we show that sputtering with low-energy Ar^+ ions can transform single-layer MoS_2 all the way to $MoS_{1.5}$, while *in situ* x-ray photoelectron spectroscopy (XPS) reveals substantially unchanged Mo 3d states. In situ monitoring of the photoluminescence (PL) allows us to gauge the impact of the sputter-induced defects/vacancies on the exciton dynamics; in the temperature regime between 175 and 300 K we find a decay of PL yield that decreases at $\sim 7.0 \pm 0.5$ times the rate of sulfur removal.

7.2 Experiment Setup

Our measurements were performed on films and isolated islands of single-layer MoS_2 grown on a SiO_2 substrate from MoO_3 and elemental sulfur, as described elsewhere [164]. Figure 1(a) shows an optical microscopy image of a representative area of a MoS_2 film used in this study. Figure 1(b) is a schematic representation of the structure of single-layer MoS_2, which consists of hexagonal top and bottom layers of sulfur surrounding a molybdenum layer. The samples were characterized in air prior to our experiments using Raman and PL spectroscopy. The right portion of the image in figure 1(a) shows a continuous film of monolayer thickness, while the left area consists of single-layer MoS_2 islands. Both regions exhibit the same PL peak at 1.87 eV, corresponding to the direct band gap. Raman spectra reveal the E^1_{2g} and A_{1g} modes, with a separation of 21 cm^{-1}, as is typically seen in single-layer MoS_2 films prepared by CVD [144, 165].

Once a sufficiently homogeneous area of the MoS_2 film exhibiting exclusively single-layer Raman and PL characteristics had been identified, the sample was attached to a temperature-controlled manipulator in an ultra-high vacuum system. For subsequent studies of sputtering, the system was evacuated and baked to reach a base pressure of 1×10^{-9} Torr. A Varian sputter gun operated at 500 V acceleration potential, 20 mA emission current, and $5 \times 10^{-6} 2 \times 10^{-5}$ Torr partial pressure of Ar was used for generating Ar^+ ions. The sputter beam had a diameter of 0.5 cm. For reference, we measured the sputter current induced by this beam on a copper surface as $0.62.2\mu A$, respectively, for the Ar pressures given above. In the following, we will assume this value as an approximation of the beam current.

The XPS measurements were performed using excitation by Al Kα radiation with the emitted electrons detected by a Scienta R300 hemispheric analyzer equipped with a 2D detector. The PL experiments employed a Spectra Physics Millennia laser operating at a wavelength of 532 nm, a spectrometer with 1200 lines mm^{-1} grating blazed at 750 nm, and a liquid-nitrogen cooled Princeton Instruments SPEC-10 CCD detector. For *insitu* measurements a 50 mm focal length lens inside our UHV system was used to focus $\sim$ 100 mW of pump beam onto the sample surface with a spot of $\sim 100\mu m$. This results in an intensity of approximately $10\mu W \mu m^{-2}$, similar to that of typical microscope-based Raman measurements

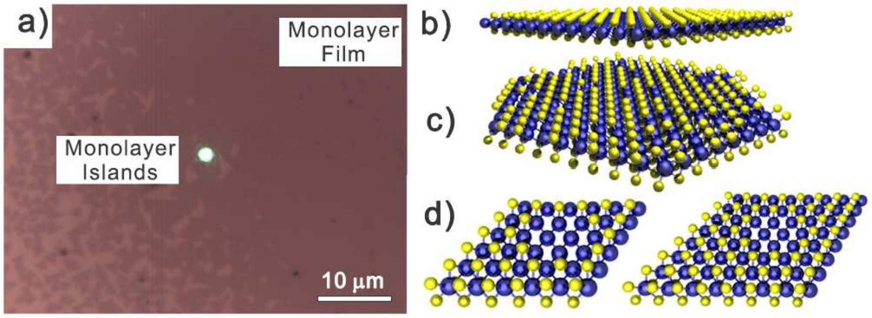

Figure 7.1: (a) Optical micrograph of the type of MoS_2 films used in this study, with single-layer islands on the left and a continuous single-layer film on the right of the imaged area. The laser spot is 2μm in size and was used for measurement of Raman spectra in air. (b) The structure of an ideal MoS_2 monolayer film, consisting of a plane of Mo atoms surrounded by two planes of S atoms. (c) A representation of a possible structure of the film after sputter removal of 12.5% of its sulfur (25% of the top-layer sulfur atoms). (d) A compact 7-atom top-layer sulfur vacancy in the two computational supercells used in this work. These structures were found to be stable within our ab initio molecular dynamics simulation at 350 K.

[132]. We collected the resultant PL signal in the back-scattered direction using a dichroic mirror to separate the excitation beam from PL signal.

Vacancy formation energy and thermal stability of the sputtered film was evaluated using the Vienna *ab initio* simulation package (VASP) [107,109] to perform density functional theory (DFT) simulations.We employed projectoraugmented wave (PAW) [114, 115] and plane-wave basis set methods. We used the PerdewBurkeErnzerhof of functional (PBE) [111] to describe exchange correlation interactions and adopted a cut-off for plane-wave expansion at 500 eV. The conjugate-gradient algorithm [166] was employed for structural relaxation and to optimize lateral atomic coordinates by minimizing the in-plane components of the stress tensor; relaxation was allowed with periodic boundary conditions until all components of the force reached a value below 0:01 eV $\mathring{A}^{-1}$. Given the large number of atoms in the computational supercell (up to 192), we found sampling of the Brillouin zone with one k-point to be adequate for evaluation of the total energy. *Ab initio* molecular dynamic (MD) simulations utilized the Nosé algorithm [167] for setting the system temperature and a 3 fs time step. To minimize the computational cost, the cut-off for plan-wave expansion was reduced to 300 eV and the simulations ran for a total time of 12 ps.

Our measurements involved cycles of sputtering at room temperature, in situ acquisition of XPS spectra of the Mo 3d, the S 2p, and the Si 2s levels, as well as *insitu* PL measurement at variable temperature. To avoid sample degradation, all experiments were conducted in immediate succession to one another, with the sample maintained in ultra-high vacuum. Figures 2(a)(c) displays the evolution of XPS spectra during sputtering at 2×10^{-5} Torr Ar pressure, corresponding to a net sputter current of $2.2 \mu A$. Figure 2(a) shows representative spectra of the Mo 3d 3/2 and 5/2 peaks for increasing sputter times. The sulfur 2s peak is also visible on the low-energy side of the Mo-derived features. We observe no appreciable reduction in Mo 3d intensity. Further, the shape of the Mo 3d 3/2 and 5/2 doublet remains essentially unchanged, as is best seen in the energy-aligned superposition below the individual spectra in figures 2(a) and (b). In order to account for potential charging of the MoS_2 sample on the thick oxide layer, we treat the Si 2p peak (figure 2(c)) as a standard and reference all other states to it. Figure 2(d) shows the evolution of the Mo 3d intensity as a function of sputter time.

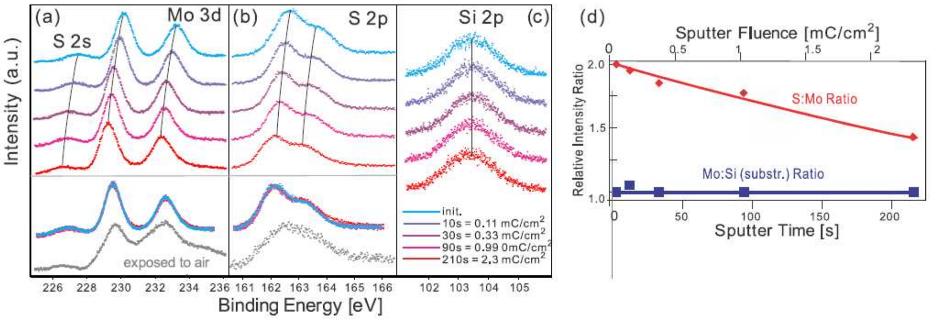

Figure 7.2: XPS spectra of (a) the Mo 3d 3/2 and 5/2 states, as well as the S 2s (weak features on the left), (b) the S 2p state, and (c) the Si 2p state. The spectra (from the top to the bottom) were acquired after increasing amounts of sputtering. To account for surface charging, the spectra at different sputter times were aligned so that the Si 2s peak remains at constant energy. The lower parts of (a) and (b) show spectra scaled and shifted for the best overlay of the peak shape, as well as the corresponding spectra after exposure to air. (d) The evolution during sputtering of the intensity of the Mo XPS signal referenced to the substrate Si peak and normalized to unity, and the S:Mo XPS ratio normalized to 2. While the Mo content is seen to remain essentially constant, the amount of sulfur decreases significantly during sputtering.

7.3 Result and Analysis

The sulfur signal (figure 2(b)), in contrast to the Mo 3d feature, exhibits a significant reduction in strength from sputtering, with little change of the overall peak shape. Figure 2(d) shows that the total sulfur content, normalized to 2 for the unsputtered film to account for the different XPS yields of the Mo and S states, decreases with sputter time. Within the duration of this experiment, we observe a reduction of the sulfur content of the film by 25%, or 50% of the top sulfur layer in the MoS_2 structure (figure 1(b)). This corresponds to an average sputter yield of 0.03 per Ar^+ ion. A first-order approximation of the sulfur signal decay (red line in figure 2(d)) corresponds to an exponential fit with a rate constant of $1.6 \times 10^{-3} 1 s^{-1}$ or $1.4 \times 10^{-4} cm^2 C^{-1}$.

We ascribe the selectivity to sulfur removal to the close mass match between the Ar^+ ions and the sulfur atoms, as well as to the low Ar^+ energy; 3 keV Ar^+ ions are capable of removing Mo completely from our substrates. The silicon peak (figure 2(c)) serves as an internal reference and is not significantly affected by sputtering or exposure to air.

Apart from a shift to lower binding energy, likely arising from charging of the sputtered MoS_2 film with respect to the underlying SiO_2 layer, we observe little change of the peak shape of the Mo- and S-derived features (lower part of figures 2(a) and (b)). The latter suggests that despite sputtering, the MoS_2 film retains its homogeneity and its overall MoS_2 structure; we speculate that this is achieved by the presence of an unperturbed bottom sulfur layer that retains the structure of the Mo layer rigid, despite the absence of some of the top-layer sulfur atoms. We further support this argument in the following paragraphs.

Prior to processing, the sulfur and the molybdenum coverage of the samples correlate with one another. There is neither a significant quantity of sulfur in the absence of molybdenum nor is there appreciable incorporation of sulfur into the substrate surface during preparation. We reach these conclusions by aligning the sample so that the spatially resolved axis of our 2D detector lies along the horizontal of figure 1(a), i.e., by detecting the XPS yield from sample areas covered by a thick MoS_2 film on one side (where we find strong signal both for S and Mo), across an area with MoS_2 islands (where we find reduced signals for both S and Mo), and ending at a sample area devoid of MoS_2 features on the other side (where we find neither significant Mo nor S signal). This observation indicates that the S/Mo ratio that we track in the XPS-sputter cycles can indeed be related to modification of the MoS_2 monolayer and is not significantly affected by any other possible sulfur source in the surface region. The fact that the MoS_2 film is the material being modified is further buttressed by the films dramatic change in stability after processing. XPS measurement on a sputtered film after exposure to air exhibit significantly broadening Mo 3d 3/2 and 5/2 peaks, as well as S 2p peaks (bottom of figures 2(a) and (b)). We attribute this to extensive oxidation. After sputtering and air exposure, atomic force microscopy reveals degradation in film smoothness, and the films Raman response is significantly reduced. On the other hand, the original, unprocessed films are found to be stable in air.

To confirm that a MoS_2 film with a significant fraction of its top sulfur atoms removed is structurally stable in vacuum for the temperature range of our measurements ($\leq$350 K), we performed DFT calculations on (6×6) and (8×8) MoS_2 units supercells from which we removed a hexagon of 7 adjacent top-layer sulfur atoms (figure 1(d)). Such an arrangement allows us to examine the effect of creation of a relatively large vacancy cluster on the stability of the single-layer MoS_2. Structural relaxation maintains the overall shape of the film and changes the original MoMo bond length inside the S-depleted region $\leq 5\%$. Allowing the film to evolve at 350 K over a 12 ps interval within *ab initio* MD leads to no structural change of the film, further supporting the stability of such a sulfur-depleted structure. We note that our calculations do not account for the support of the film structure through an underlying substrate and assume a comparatively large region of depletion of the surface sulfur. Both of these effects generate higher strain than is likely present in the films under experimental conditions.

To explore the impact of sputtering on the optical response of our films, we performed *in situ* PL measurements. Figures 3(a) and (b) show PL spectra acquired at temperatures of

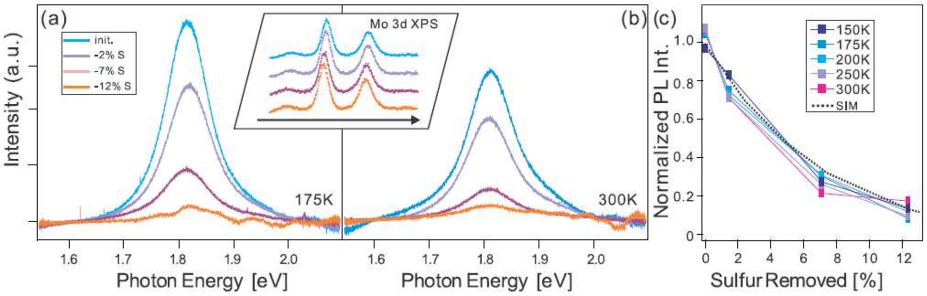

Figure 7.3: PL spectra of a MoS_2 sample for increasing sputter time/sulfur depletion recorded at temperatures of (a) 175 K and (b) 300 K. The inset shows the corresponding Mo 3d 3/2 and 5/2 XPS spectra, which remain virtually unchanged. At higher temperatures, a lower initial PL yield is observed; during sputter removal of sulfur the PL yield decreases at both temperatures. (c) The normalized intensity of the PL signal as a function of the percentage of total sulfur removed for different indicated temperatures. The dotted line (sim) corresponds to the model described in the text.

175 and 300 K. In both cases, we observe a clear PL signal prior to sputtering, which decays with sputter exposure. The inset of figures 3(a) and (b) shows the Mo 3d XPS spectra acquired at 300 K at each of the sputter times, which are virtually unchanged throughout the experiment. By comparison of their intensity to the sulfur XPS intensity (not shown), we obtain the amount of sulfur removed. In addition, we observe a well-known reduction of PL yield with increasing temperature [45].

We fitted each PL peak with a Gaussian curve and a constant background. Figure 3(c) shows the evolution of the Gaussian amplitude with sputter time. For purposes of comparison, we plot the relative evolution of the PL yield for each temperature as a function of the reduction in sulfur content of the film (figure 3(c)).

The PL yield decreases as sulfur is removed. For 10% of sulfur depletion, the PL yield is reduced by almost 80%, i.e., an average decrease of $\sim (7.0 \pm 0.5)\times$ the rate of decrease of the sulfur concentration. Note that in figure 3 and in our discussion the fraction of sulfur is referred to the overall sulfur content of the MoS_2 monolayer structure. As sputtering is far more likely to remove sulfur in the top layer than in the bottom sulfur layer, the percentage values are twice as high if referred only to the top sulfur layer. As seen in figure 3(c), the quenching behavior of the PL is largely unchanged over the temperature regime addressed in this study.

The exciton dynamics underlying the quenching of the PL by sputtering is likely complicated. A rigorous treatment has to account for changes to the MoS_2 band structure, absorbance, and charging, which is beyond the scope of this study. However, we note that good agreement with the data can be achieved if one assumes (a) that the MoS_2 single-layer absorbance is not significantly changed by sputtering, (b) that quenching occurs whenever a photon is absorbed in a MoS_2 unit cell that is perturbed, i.e., missing its top sulfur atom or missing lateral coordination due to a sulfur atom being removed from a directly adjacent unit cell, and (c) that in all other cases the PL yield is identical to the that of the unperturbed system. To obtain values for the PL quenching from these assumptions we have performed a simple simulation (dotted line in figure 3(c)). Using a MoS_2 film of 200 × 200 unit cells, we randomly remove a varying fraction of the top-layer sulfur atoms and evaluate for 1000 arbitrarily chosen locations whether or not the unit cell is perturbed (as defined above). While this model provides agreement with the experiment, we note that a combination of less than unity quenching efficiency of defects and longer exciton diffusion lengths would yield similar overall behavior [165].

7.4 Conclusion

In summary, we have shown that sputtering with a beam of low-energy argon ions provides a method for selective desulfurization of monolayer MoS_2. The spectroscopic studies and DFT modeling suggest that the basic physical structure of the MoS_2 remains largely intact as the sulfur is removed. Our findings suggest that low-energy argon sputtering may have significant potential for the activation, functionalization, and modification of MoS_2 layers. Although not studied systematically, the sharp increase in reactivity of the processed MoS_2 monolayer is apparent from its rapid oxidation in air.

Reference

[1] Q Ma, PM Odenthal, J Mann, D Le, CS Wang, Y Zhu, T Chen, D Sun, K Yamaguchi, *Journal of Physics: Condensed Matter* 25 (25), 252201

[2] Zhu, Y., Wyrick, J., Cohen, K., Magnone, K., Holzke, C., Salib, D., Ma, Q., Sun, D. and Bartels, L. *Journal of Physics: Condensed Matter,* 24, 354005 (2012)

[3] Luo, M., Lu, W., Kim, D., Chu, E., Wyrick, J., Holzke, C., Salib, D., Cohen, K., Cheng, Z., Sun, D., Zhu, Y., Einstein, T., Bartels, L., *Journal of Chemical Physics,* 135*,* 134705 (2011)

[4]Kim, D., Sun, D., Lu, W., Cheng, Z., Zhu, Y., Le, D., Rahman, T.S. & Bartels, L. *Langmuir,* 27, 11650 (2011)

[5] Wyrick, J., Kim, D.H., Sun, D., Cheng, Z., Berland, K., Kim, Y.S., Rotenberg, E., Lu, W., Zhu, Y., Luo, M., Hyldgaard, P., Einstein, T.L., Bartels, L., *Nano Letters,* 11, 2944 (2011)

[6] Cheng Z., Chu E., Sun, D., Kim D., Zhu Y., Luo M., Pawin G., Lu W., Wong K.L., Kwon K.Y., Carp R., Marsella M., Bartels L*, Journal of The American Chemical Society,* 132, 13578 (2010)

[7] Sun D., Kim D., Le D., Borck Ø., Berland K., Kim K., Lu W., Zhu Y., Luo M., Wyrick J., Cheng Z., Einstein T.L., Rahman T.S., Hyldgaard P., Bartels L*., Physical Review B,* 82, 201410 (2010)

[8] Cheng Z., Luo M., Wyrick J., Sun, D., Kim D., Zhu Y., Lu W., Kim K., Einstein T.L., Bartels L*., Nano Letters,* 10, 1022018 (2010)

[9] Cheng Z., Wyrick J., Luo M., Sun, D., Kim D., Zhu Y., Lu W., Kim K., Einstein T.L., Bartels L*., Physical Review Letters,* 105, 066104 (2010)

[10]C. Bai (2000). *Scanning tunneling microscopy and its applications*. New York: Springer Verlag. ISBN 3-540-65715-0.

[11]STM References - Annotated Links for Scanning Tunneling Microscope Amateurs". Retrieved July 13, 2012.

[12]Serway; Vuille (2008). *College Physics* **2** (Eighth ed.). Belmont: Brooks/Cole. ISBN 9780495554752.

[13] http://hyperphysics.phy-astr.gsu.edu/hbase/quantum/barr.html

[14] D. Sun, Thin Film Morphology Control by Mechanical, Electronic and Chemical Interactions: a Scanning Tunneling Microscopy and Photoelectron Spectroscopy Study. [Ph.D. dissertation], University of California, Riverside (2012).

[15] M. Luo, An STM Study of Molecular Self-Assemblies on Cu(111): Structure, Interaction, and Effects of Confinement [Ph.D. dissertation], University of California, Riverside (2012).

[16] D. Kim, STM Study of Dynamics and Pattern Formations of Adsorbates on Copper (111) [Ph.D. dissertation], University of California, Riverside (2011).

[17] G. Pawin, Molecular diffusion, energetics, and structures on copper(111) as studied by scanning tunneling microscopy [Ph.D. dissertation], University of California, Riverside (2008).

[18] X. Lin, Molecular machinery [Ph.D. dissertation], University of California, Riverside (2007).

[19] K.-Y. Kwon, Reactivity, dynamics, and film formation of arenethiols studied by STM [Ph.D. dissertation], University of California, Riverside (2005).

[20] J.J. Sakurai and J. Napolitano, *Modern Quantum Mechanics*, Addison-Wesley (2010).

[21] C.J. Chen, *Introduction to Scanning Tunneling Microscopy*, Oxford UK (2007).

[22] G. Binnig and H. Rohrer, *HELV PHYS ACTA* **55** (1982) (6), p. 726.

[23] M. Baumer and H.J. Freund, *Prog. Surf. Sci.* **61** (1999) (7-8), p. 127.

[24] F. Nouvertne, U. May, A. Rampe, M. Gruyters, U. Korte, R. Berndt and G. Güntherodt, *Surf. Sci.* **436** (1999) (1-3), p. L653.

[25] L. Bartels, S. Hla, A. Kuhnle, G. Meyer, K. Rieder and J. Manson, *Phys. Rev. B* **67** (2003) (20), p. 205416.

[26] L. Lauhon and W. Ho, *Surf. Sci.* **451** (2000) (1-3), p. 219.

[27] Z. Song, J. Pascual, H. Conrad, K. Horn and H. Rust, *Surf. Sci.* **491** (2001) (1-2), p. 39.

[28] Y.F. Wang, J. Kroger, R. Berndt and W. Hofer, *Angew. Chem. Int. Ed. Engl.* **48** (2009) (7), p. 1261.

[29] L. Bartels, G. Meyer and K. Rieder, *Chem. Phys. Lett.* **273** (1997) (5-6), p. 371.

[30] L. Bartels, G. Meyer and K. Rieder, *Phys. Rev. Lett.* **79** (1997) (4), p. 697.

[31] L. Bartels, G. Meyer and K. Rieder, *J VAC SCI TECHNOL A* **16** (1998) (3), p.1047.

[32] L. Bartels, G. Meyer, K. Rieder, D. Velic, E. Knoesel, A. Hotzel, M. Wolf and G. Ertl, *Phys. Rev. Lett.* **80** (1998) (9), p. 2004.

[33] L. Bartels, B. Rao and A. Liu, *Chem. Phys. Lett.* **385** (2004) (1-2), p. 36.

[34] A. Deshpande, H. Yildirim, A. Kara, D.P. Acharya, J. Vaughn, T.S. Rahman and S.W. Hla, *Phys. Rev. Lett.* **98** (2007) (2), p. 028304

[35] J. Li, W. Schneider and R. Berndt, *Appl. Phys. A - Mater.* **66** (1998), p. S675.

[36] G. Meyer, S. Zophel and K. Rieder, *Appl. Phys. A - Mater.* **63** (1996) (6), p. 557.

[37] J. Bardeen, *Phys. Rev. Lett.* **6** (1961) (2), p. 57.

[38] J. Tersoff and D.R. Hamann, *Phys. Rev. Lett.* **50** (1983) (25), p. 1998.

[39]Sedra, Adel; Smith, Kenneth C. (1991). *Microelectronic Circuits, 3 ed*. Saunders College Publishing. p. 60. ISBN 0-03-051648-X.

[40]Jacob Millman, *Microelectronics: Digital and Analog Circuits and Systems*, McGraw-Hill, 1979, ISBN 0-07-042327-X, pp. 523-527

[41] M. Haruta, *Nature* (London) 437, 1098 (2005).

[42] Pawin, G.; Wong, K. L.; Kwon, K. Y.; Bartels, L. *Science* **2006**, *313*, 961–962.

[43] Lobo-Checa, J.; Matena, M.; Muller, K.; Dil, J. H.; Meier, F.; Gade, L. H.; Jung, T. A.; Stohr, M. *Science* **2009**, *325*, 300–303.

[44] Bartels, L. *Nat. Chem.* **2010**, *2*, 87–95.

[45] M. Corso et al., Science 303, 217 (2004).

[46] Heller, E.; Crommie, M.; Lutz, C.; Eigler, D. *Nature* **1994**, *369*,464–466.

[47] M.V. Rastei et al., Phys. Rev. Lett. 99, 246102 (2007).

[48] Theobald, J. A.; Oxtoby, N. S.; Phillips, M. A.; Champness, N. R.; Beton, P. H. *Nature* **2003**, *424*, 1029–1031.

[49] Berner, S.; Corso, M.; Widmer, R.; Groening, O.; Laskowski, R.; Blaha, P.; Schwarz, K.; Goriachko, A.; Over, H.; Gsell, S.; Schreck, M.; Sachdev, H.; Greber, T.; Osterwalder, J. *Angew. Chem., Int. Ed. Engl.* **2007**, *46*, 5115–5119.

[50] M. Gsell, P. Jakob, and D. Menzel, Science 280, 717 (1998).

[51] Stranick S J, Kamna M M and Weiss P S 1994 Atomic-scaledynamics of a two-dimensional gas–solid interface Science 266 99–102

[52] N. N. Negulyaev et al., Phys. Rev. Lett. 101, 226601 (2008).

[53] Sykes E C H, Han P, Kandel S A, Kelly K F, McCarty G S and Weiss P S 2003 Substrate–mediated interactions and intermolecular forces between molecules adsorbed on surfaces Acc. Chem. Res. 36 945–53

[54] Nanayakkara S U, Sykes E C H, Fernandez-Torres L C, Blake M M and Weiss P S 2007 Long-range electronic interactions at a high temperature: bromine adatom islands on Cu(111) Phys. Rev. Lett. 98 206108

[55] Lukas S, Witte G and Woll C 2002 Novel mechanism for molecular self-assembly on metal substrates: unidirectional rows of pentacene on Cu(110) produced by a substrate–mediated repulsion Phys. Rev. Lett. 88 028301

[56] Wong, K. L.; Rao, B. V.; Pawin, G.; Ulin-Avila, E.; Bartels, L. *J. Chem. Phys.* **2005**, *123*, 201102.

[57] Mitsui, T.; Rose, M. K.; Fomin, E.; Ogletree, D. F.; Salmeron, M. *Phys. Rev. Lett.* **2005**, *94*, No. 036101.

[58] Repp, J.; Moresco, F.; Meyer, G.; Rieder, K.; Hyldgaard, P.; Persson, M. *Phys. Rev. Lett.* **2000**, *85*, 2981–2984.

[59] T. L. Einstein, in Physical Structure of Solid Surfaces, Handbook of Surface Science, edited by W. N. Unertl (Elsevier, New York, 1996), Vol. 1, p. 577-650.

[60] Fichthorn K and Scheffler M 2000 Island nucleation in thin-film epitaxy: a first-principles investigation Phys. Rev. Lett. 84 5371–4

[61] O¨ sterlund L, Pedersen M, Stensgaard I, Laesgaard E and Besenbacher F 1999 Quantitative determination of adsorbate–adsorbate interactions Phys. Rev. Lett. 83 4812–5

[62] V. Stepanyuk et al., Phys. Rev. B 68, 205410 (2003).

[63] Wang Y F, Ge X, Manzano C, Korger J, Berndt R, Hofer W A, Tang H and Cerda J 2009 Supramolecular patterns controlled by electron interference and direct intermolecular interactions J. Am. Chem. Soc. 131 10400–2

[64] T. T. Tsong and R. Casanova, Phys. Rev. B 24, 3063 (1981).

[65] G. L. Kellogg, Surf. Sci. Rep. 21, 1 (1994).

[66] H.W. Fink and G. Ehrlich, J. Chem. Phys. 81, 4657 (1984).

[67] Kulawik, M.; Rust, H. P.; Heyde, M.; Nilius, N.; Mantooth, B. A.; Weiss, P. S.; Freund, H. J. *Surf. Sci.* **2005**, *590*, L253–L258.

[68] Hyldgaard, P.; Einstein, T. L. *Europhys. Lett.* **2002**, *59*, 265–271.

[69] A. Bogicevic et al., Phys. Rev. Lett. 85, 1910 (2000).

[70] Bartels, L.; Meyer, G.; Rieder, K. *Appl. Phys. Lett.* **1997**, *71*, 213–215.

[71] See supplementary material at http://link.aps.org/supplemental/10.1103/PhysRevLett.105.066104.

[72] Fiete, G. A.; Heller, E. J. *Rev. Mod. Phys.* **2003**, *75*, 933–948.

[73] J. Mathews and R. L. Walker, Mathematical Methods of Physics (W.A. Benjamin, New York, 1970).

[74] L. Gross et al., Phys. Rev. Lett. 93, 056103 (2004).

[75] K. E. Atkinson and W. Han, Elementary Numerical Analysis (John Wiley & Sons, New York, 2004).

[76] A. Kiełbasin´ski and H. Schwetlick, Numerische Lineare Algebra: Eine Computerorientierte Einfu¨hrung (Harri Deutsch, Thun, 1988).

[77] Kevan S D and Gaylord R H 1987 High-resolution photoemission study of the electronic structure of the noble-metal (111) surfaces Phys. Rev. B 36 5809–18

[78] L. Burgi et al., Surf. Sci. 447, L157 (2000).

[79] Haruta, M.; Kobayashi, T.; Sano, H.; Yamada, N. *Chem. Lett.* **1987**,405–408.

[80] Chen, M. S.; Goodman, D. W. *Science* **2004**, *306*, 252–255.

[81] Somorjai, G. A. *Introduction to surface chemistry and catalysis*; Wiley: New York, 1994.

[82] Mantooth, B. A.; Sykes, E. C. H.; Han, P.; Moore, A. M.; Donhauser, Z. J.; Crespi, V. H.; Weiss, P. S. *J. Phys. Chem. C* **2007**, *111*, 6167–6182.

[83] Han, P.; Mantooth, B.; Sykes, E.; Donhauser, Z.; Weiss, P. *J. Am.Chem. Soc.* **2004**, *126*, 10787–10793.

[84] Sachs, C.; Hildebrand, M.; Volkening, S.; Wintterlin, J.; Ertl, G. *Science* **2001**, *293*, 1635–1638.

[85] Hendriksen, B.; Bobaru, S.; Frenken, J. *Surf. Sci.* **2004**, *552*, 229–242.

[86] Tierney, H. L.; Baber, A. E.; Sykes, E. C. H. *J. Phys. Chem. C* **2009**, *113*, 7246–7250.

[87] Briner, B.; Doering, M.; Rust, H.; Bradshaw, A. *Science* **1997**, *278*,257–260.

[88] Heinrich, A.; Lutz, C.; Gupta, J.; Eigler, D. *Science* **2002**, *298*, 1381–1387.

[89] Longwitz, S.; Schnadt, J.; Vestergaard, E.; Vang, R.; Laegsgaard, E.; Stensgaard, I.; Brune, H.; Besenbacher, F. *J. Phys. Chem. B* **2004**, *108*, 14497–14502.

[90] Stepanow, S.; Lingenfelder, M.; Dmitriev, A.; Spillmann, H.; Delvigne, E.; Lin, N.; Deng, X. B.; Cai, C. Z.; Barth, J. V.; Kern, K. *Nat. Mater.* **2004**, *3*, 229–233.

[91] Decker, R.; Schlickum, U.; Klappenberger, F.; Zoppellaro, G.; Klyatskaya, S.; Ruben, M.; Barth, J. V.; Brune, H. *Appl. Phys. Lett.* **2008**, *93*, 243102.

[92] Otero, R.; Rosei, F.; Naitoh, Y.; Jiang, P.; Thostrup, P.; Gourdon, A.; Laegsgaard, E.; Stensgaard, I.; Joachim, C.; Besenbacher, F. *Nano Lett* **2004**, *4*, 75–78.

[93] Kulawik, M.; Rust, H.-P.; Heyde, M.; Nilius, N.; Mantooth, B. A.; Weiss, P. S.; Freund, H.-J. *Surf. Sci.* **2005**, *590*, L53.

[94] Bartels, L.; Meyer, G.; Rieder, K. *Surf. Sci.* **1999**, *432*, L621–L626.

[95] Shan, B.; Zhao, Y. J.; Hyun, J.; Kapur, N.; Nicholas, J. B.; Cho, K. *J. Phys. Chem. C* **2009**, *113*, 6088–6092.

[96] Ennis C J, Carr P A and McCash E M 2003 Long range ordered structure of ethyne on Cu(111) Surf. Sci. 539 L574–6

[97] Christensen C H, Rass-Hansen J, Marsden C C,Taarning E and Egeblad K 2008 The renewable chemicals industry ChemSusChem 1 283–9

[98] Bao S, Schindler K M, Hofmann P, Fritzsche V, Bradshaw A M and Woodruff D P 1993 The local adsorption structure of acetylene on Cu(111) Surf. Sci. 291 295–308

[99] Hermann K and Witko M 1995 Geometry and binding of acetylene on Cu(111): ab initio cluster studies Surf. Sci. 337 205–14

[100] Konishi Y, Sainoo Y, Kanazawa K, Yoshida S, Taninaka A, Takeuchi O and Shigekawa H 2005 Tunneling spectroscopy and manipulation of a single C2H2 molecule on a Cu(111) surface Phys. Rev. B 71 193410

[101] Stipe B, Rezaei M and Ho W 1998 Single-molecule vibrational spectroscopy and microscopy Science 280 1732–5

[102] Eigler D, Lutz C and Rudge W 1991 An atomic switch realized with the scanning tunneling microscope Nature 352 600–3

[103] Neu B, Meyer G and Rieder K 1995 Controlled vertical and lateral manipulation of single atoms and molecules with the scanning tunneling microscope Mod. Phys. Lett. B 9 963–9

[104] Hahn J and Ho W 2001 Single molecule imaging and vibrational spectroscopy with a chemically modified tip of a scanning tunneling microscope Phys. Rev. Lett. 8719 196102

[105] Gross L, Moll N, Mohn F, Curioni A, Meyer G, Hanke F and Persson M 2011 High-resolution molecular orbital imaging using a p-wave STM tip Phys. Rev. Lett. 107 086101

[106] Gingery D and Buhlmann P 2011 Voltage-induced chemical contrast in scanning tunneling microscopy using tips chemically modified with hydrogen bond donors Surf. Sci. 605 1099–102

[107] Kresse G and Hafner J 1993 Ab initio molecular-dynamics for liquid-metals Phys. Rev. B 47 558–61

[108] Kresse G and Hafner J 1994 Ab initio molecular-dynamics simulation of the liquid-metal amorphous-semiconductor transition in germanium Phys. Rev. B 49 14251–69

[109] Kresse G and Furthmuller J 1996 Efficiency of ab initio total energy calculations for metals and semiconductors using a plane-wave basis set Comput. Mater. Sci. 6 15–50

[110] Kresse G and Furthmuller J 1996 Efficient iterative schemes for ab initio total-energy calculations using a plane-wave basis set Phys. Rev. B 54 11169–86

[111] Perdew J P, Burke K and Ernzerhof M 1996 Generalized gradient approximation made simple Phys. Rev. Lett. 77 3865–8

[112] Perdew J P, Burke K and Ernzerhof M 1996 Generalized gradient approximation made simple Phys. Rev. Lett. 77 3835

[113] Perdew J P, Burke K and Ernzerhof M 1997 Phys. Rev. Lett. 78 1396 (erratum)

[114] Blochl P E 1994 Projector augmented-wave method Phys. Rev. B 50 17953–79

[115] Kresse G and Joubert D 1999 From ultrasoft pseudopotentials to the projector augmented-wave method Phys. Rev. B 59 1758–75

[116] Tersoff J and Hamann D R 1985 Theory of the scanning tunneling microscope Phys. Rev. B 31 805–13

[117] Sautet P and Bocquet M L 1994 A theoretical-analysis of the site dependence of the shape of a molecule in STM images Surf. Sci. 304 L445–450

[118] Pedersen M, Bocquet M, Sautet P, Laegsgaard E, Stensgaard I and Besenbacher F 1999 CO on Pt(111): binding site assignment from the interplay between measured and calculated STM images Chem. Phys. Lett. 299 403–9

[119] Tiwari R K, Otalvaro D M, Joachim C and Saeys M 2009 Origin of the contrast inversion in the STM image of CO on Cu Surf. Sci. 603 3286–91

[120] Nieminen J, Niemi E, Simic-Milosevic V and Morgenstern K 2005 STM images and tunneling channels of substituted benzene molecules Phys. Rev. B 72 195421

[121] Luo M et al 2011 Coalescence of 3-phenyl-propynenitrile on Cu(111) into interlocking pinwheel chains J. Chem. Phys. 135 134705

[122] Knorr N, Brune H, Epple M, Hirstein A, Schneider M and Kern K 2002 Long-range adsorbate interactions mediated by a two-dimensional electron gas Phys. Rev. B 65 115420

[123] Wyrick J et al 2011 Do two-dimensional ‘noble gas atoms’ produce molecular honeycombs at a metal surface? Nano Lett. 11 2944–8

[124] Silly F, Pivetta M, Ternes M, Patthey F, Pelz J P and Schneider W D 2004 Creation of an atomic superlattice by immersing metallic adatoms in a two-dimensional electron sea Phys. Rev. Lett. 92 016101

[125] Stepanyuk V S, Niebergall L, Baranov A N, Hergert W and Bruno P 2006 Long-range electronic interactions between adatoms on transition metal surfaces Comput. Mater. Sci. 35 272–4

[126] Han P and Weiss P S 2012 Electronic substrate–mediated interactions Surf. Sci. Rep. 67 19–81

[127] Hyldgaard P and Persson M 2000 Long-ranged adsorbate-adsorbate interactions mediated by a surface-state band J. Phys.: Condens. Matter 12 L13–9

[128] Berland K, Einstein T L and Hyldgaard P 2012 Response of the Shockley surface state to an external electrical field: a density-functional theory study of Cu(111) Phys. Rev. B85 035427

[129] Butler S Z et al 2013 ACS Nano 7 2898–926

[130] Wang Q H, Kalantar-Zadeh K, Kis A, Coleman J N and Strano M S 2012 Nature Nanotechnol. 7 699

[131] Chhowalla M, Shin H S, Eda G, Li L-J, Loh K P and Zhang H 2013 Nature Chem. 5 263

[132] Mak K F, Lee C, Hone J, Shan J and Heinz T F 2010 Phys. Rev. Lett. 105 136805

[133] Splendiani A, Sun L, Zhang Y, Li T, Kim J, Chim C-Y, Galli G and Wang F 2010 Nano Lett. 10 1271–5

[134] Besenbacher F, Brorson M, Clausen B S, Helveg S, Hinnemann B, Kibsgaard J, Lauritsen J, Moses P G, Norskov J K and Topsoe H 2008 Catal. Today 130 86

[135] Kisielowski C, Ramasse Q M, Hansen L P, Brorson M, Carlsson A, Molenbroek A M, Topsoe H and Helveg S 2010 Angew. Chem. Int. Edn 49 2708

[136] Li Y G, Wang H L, Xie L M, Liang Y Y, Hong G S and Dai H J 2011 J. Am. Chem. Soc. 133 7296

[137] Kibsgaard J, Chen Z B, Reinecke B N and Jaramillo T F 2012 Nature Mater. 11 963

[138] Radisavljevic B, Radenovic A, Brivio J, Giacometti V and Kis A 2011 Nature Nanotechnol. 6 147

[139] Ghatak S, Pal A N and Ghosh A 2011 ACS Nano 5 7707

[140] Late D J, Liu B, Matte H S S R, Dravid V P and Rao C N R 2012 ACS Nano 6 5635

[141] Liu K-K et al 2012 Nano Lett. 12 1538

[142] Li H, Yin Z, He Q, Li H, Huang X, Lu G, Fam D W H, Tok A I Y, Zhang Q and Zhang H 2012 Small 8 63

[143] Yin Z, Li H, Li H, Jiang L, Shi Y, Sun Y, Lu G, Zhang Q, Chen X and Zhang H 2011 ACS Nano 6 74

[144] Zhan Y, Liu Z, Najmaei S, Ajayan P M and Lou J 2012 Small 8 966

[145] Zhang Y, Ye J, Matsuhashi Y and Iwasa Y 2012 Nano Lett.12 1136

[146] Xiao D, Liu G-B, Feng W, Xu X and Yao W 2012 Phys. Rev. Lett. 108 196802

[147] Zeng H, Dai J, Yao W, Xiao D and Cui X 2012 Nature Nanotechnol. 7 490

[148] Mak K F, He K, Shan J and Heinz T F 2012 Nature Nanotechnol. 7 494

[149] Cao T et al 2012 Nature Commun. 3 887

[150] Cao T, Feng J, Shi J, Niu Q and Wang E 2012 arXiv:1112.4013

[151] Novoselov K, Jiang D, Schedin F, Booth T, Khotkevich V, Morosov S and Geim A 2005 Proc. Natl Acad. Sci. 102 10454

[152] Kim D, Sun D, Lu W, Cheng Z, Zhu Y, Le D, Rahman T S and Bartels L 2011 Langmuir 27 11650

[153] Lauritsen J V et al 2007 J. Catal. 249 220

[154] Helveg S, Lauritsen J, Lægsgaard E, Stensgaard I, Norskov J, Clausen B, Topsoe H and Besenbacher F 2000 Phys. Rev. Lett. 84 951

[155] Jaramillo T F, Jørgensen K P, Bonde J, Nielsen J H, Horch S and Chorkendorff I 2007 Science 317 100

[156] Lee Y-H et al 2012 Adv. Mater. 24 2320–5

[157] Kibsgaard J, Clausen B S, Topsøe H, Lægsgaard E, Lauritsen J V and Besenbacher F 2009 J. Catal. 263 98

[158] Kibsgaard J, Tuxen A, Levisen M, Lægsgaard E, Gemming S, Seifert G, Lauritsen J V and Besenbacher F 2008 Nano Lett. 8 3928

[159] Vilfan I 2006 Eur. Phys. J. B 51 277

[160] Sun D et al 2012 Angew. Chem. 124 10430

[161] Tiwari R K, Yang J S, Saeys M and Joachim C 2008 Surf. Sci. 602 2628

[162] Ataca C and Ciraci S 2012 Phys. Rev. B 85 195410

[163] Makarova M, Okawa Y and Aono M 2012 J. Phys. Chem. C116 22411

[164] Mann J et al 2013 Eur. Phys. J. B 86 226

[165] Zande A M V D, Huang P Y, Chenet D A, Berkelbach T C, You Y, Lee G H, Heinz T F, Reichman D R, Muller D A and Hone J 2013 Nature Mater. at press

[166] Press W H, Teukolsky S A, Vetterling W T and Flannery B P 2007 Numerical Recipes: The Art of Scientific Computing (Cambridge: Cambridge University Press) pp 515–20

[167] Nos´e S 1984 J. Chem. Phys. 81 511

[168] Tongay S, Zhou J, Ataca C, Lo K, Matthews T S, Li J, Grossman J C and Wu J 2012 Nano Lett. 12 5576